



High resolution water consumption in the Mountain Aquifer Based on SEBAL Model Earth Engine Implementation

Additional Thesis - CIE5050-09

Student

Débora da Silva Fanzeres 5458293

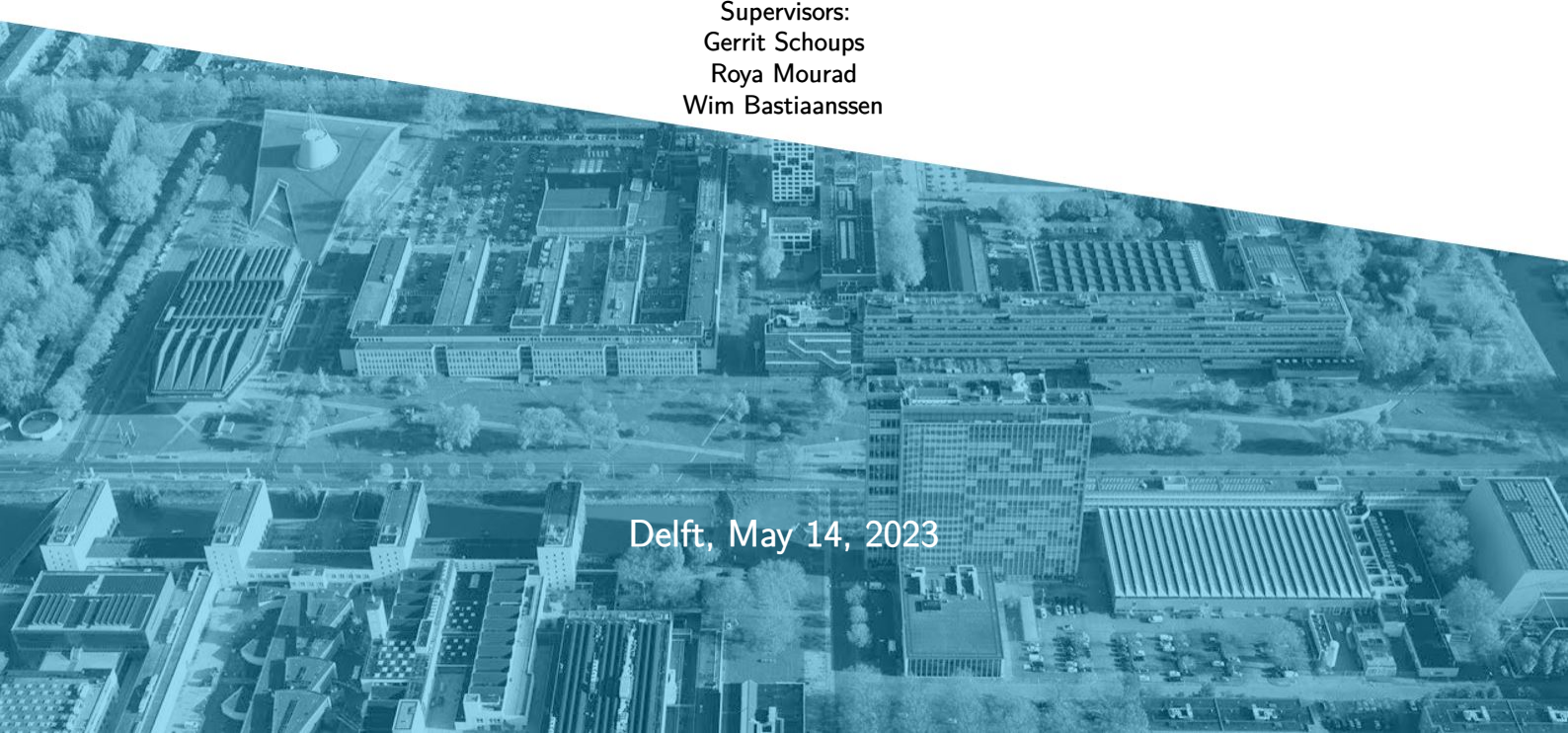
Supervisors:

Gerrit Schoups

Roya Mourad

Wim Bastiaanssen

Delft, May 14, 2023



Contents

1	Introduction	1
1.1	Study Area	1
2	Literature Review	2
2.1	Evapotranspiration in Water Management	2
2.2	Remote sensing for ET data and water balance	3
2.3	Previous studies in the Mountain Aquifer basin	7
3	Methodology	10
3.1	SEBAL algorithm	10
3.2	FAO's WaPOR product	13
3.3	Google Earth engine application	15
3.4	Data processing	16
3.5	Land use analysis	17
3.6	Comparing datas	17
4	Results and discussion	17
4.1	Actual Evapotranspiration (ETa) results	17
4.2	Limitations	23
5	Conclusion	23
6	Appendix A: Reference Evapotranspiration	28

1 | Introduction

An efficient integrated water management needs to understand the spatially distributed groundwater abstractions in the region. For transboundary basins, streams, and aquifers, it becomes even more important, as it can be a factor in political conflicts. The Mountain Aquifer is a transboundary aquifer that serves as the main source of water for Palestinians in the West Bank and is the main provider of freshwater for Israel (El-Fadel et al., 2001). Currently, the aquifer has problems such as over-abstraction and contamination, in a climate change and complex political scenario. Therefore, it is of interest for both territories to have a politically neutral assessment of groundwater recharge and abstraction so plans to improve the operations of groundwater resources can be made.

In order to facilitate a dialogue on planning groundwater allocations between Israel and the Palestinian Territories, the Government of The Netherlands asked the Delft University of Technology (TU Delft) to do a water accounting study using open-access data from satellite measurements. In order to perform the study, the water accounting system was implemented with a 250 m x 250 m grid, using the Scalable Water balance from Earth Observations (SWEO) and the UN-FAO Water Productivity Open-access portal (WaPOR) as a pre-processing tool for evapotranspiration (ET), soil moisture and dry matter production. The objective of the study was to produce a water accounting tool that provides an extra set of geographical data to the Israel and Palestinian Territories to describe the hydrological conditions.

One of the conclusions of the report is that a more accurate land use map, with 30 m pixels, can improve the understanding of the local agro-hydrological processes, such as ET, and further studies on that were recommended. A reliable estimate of ET is essential for accurate water accounting, as it is one of the most important components of the hydrological cycle. ET controls the availability and distribution of water across the surface when combined with rainfall and runoff, contributing to the surface energy balance and quantifying the water requirement (Bogawski & Bednorz, 2014; McCabe & Wood, 2006).

Even though, in many cases, there is a gap between the resolution desired and the scale in which the process can be practically represented, satellites observations are the only feasible solution to measure relatively small-scale variations in surface fluxes and states (Jackson, 1997; McCabe & Wood, 2006). Previous studies showed that higher-resolution ET data, both in terms of spatial and temporal resolutions, is necessary and a key factor for the use of the data in water management and hydrological studies (Karimi & Bastiaanssen, 2015). French et al., 2005 analyzed different modeling approaches and concluded that data for surface heat fluxes estimation, necessary for ET calculation, shows more promise for high-resolution flux mapping. Also, with higher-resolution pixels, it would be possible to understand better the consumption by crops, forests, and natural ecosystems with good spatial precision.

SEBAL (Surface Energy Balance Algorithms for Land) is a remote sensing energy balance model that can meet the requirements to produce accurate ET estimates. One of the main advantages of SEBAL for this application is the determination of actual ET on a pixel-by-pixel spatial level (Bastiaanssen et al., 2005). Previous studies also showed that WaPOR overestimated ET for irrigated areas, and the solution found was using a 30 m resolution on SEBAL to generate new ET data (Al-Bakri et al., 2022).

The present study aims to generate evapotranspiration data for the study area using 30 m pixels resolutions on a SEBAL model implemented on Earth Engine. The goal of this study is to produce data for water accounts of the Mountain Aquifer and to answer the following questions:

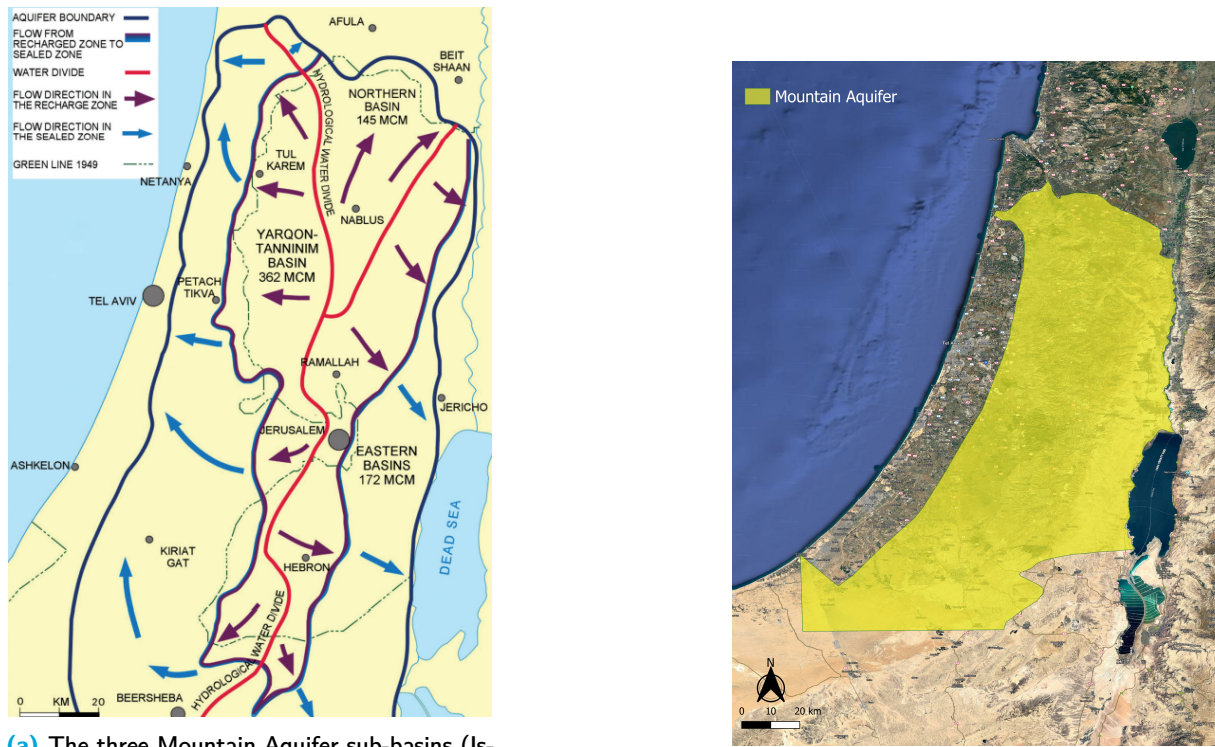
- Does using higher-resolution data on the SEBAL model for ET produce a more accurate result?
- What does the ET data produced tell about the agro-hydrological processes in the study area?

1.1 | Study Area

The area used for this study is the transboundary Mountain Aquifer, also known as Yarkon Tanninim Aquifer. It is the largest and most important water resource of the region, with an area of 10.486 km², supplying almost all of the West Bank's water requirements and one-third of Israel's water budget (El-Fadel et al., 2001). The aquifer goes through the highlands of the Westbank in the Palestinian Territory to the coastal aquifers of Israel on the west and the Jordan Rift Valley which is dominated by the Jordan River, the Sea of Galilee, and the Dead Sea, in the east. West of the Jordan Rift Valley is the Central Highlands that can exceed 1000 m in elevation in many locations and divides the groundwater system in opposite flow directions (Bastiaanssen et al., 2022).

The aquifer can be divided into three basins, based on water flow direction: the Western Aquifer Basin (WAB), the North-Eastern, and Eastern Aquifer. The Eastern aquifer flows from the mountains towards the Jordan River, while the WAB flows towards the Mediterranean Sea, and the North-Eastern Aquifer moves in

the northern direction (Bastiaanssen et al., 2022; El-Fadel et al., 2001). The entire Jordan River basin is also included from its source in Jordan and Syria to the Dead Sea, which can be useful for the present study as it is possible to check the bulk water balance for a reality check on the magnitude of ET. Figure 1.1 shows the three sub-basins of the region and the water flow path.



(a) The three Mountain Aquifer sub-basins (Israel Water Authority, 2019)

(b) Mountain Aquifer area

Figure 1.1: Study area Mountain Aquifer and the sub-basins

The aquifer is characterized by overdraft, which leads to disputes regarding accounting for groundwater abstractions and allocations. Unauthorized drilling in the region has also been cited as a problem. The aquifer potential yield varies according to the reporting source. However, safe yields of 632 million m³, including natural recharge of springs and 180 million m³ of brackish water, were estimated in consensus between Israeli and Palestinian water experts (Libiszewski, 1995). In 1995 the Oslo Agreement was established to make groundwater allocation plans based on safe yields. The data generated and available at the time can be found in Table 1.1.

Basin	Recharge SWEQ (Mm ³ /yr)		Recharge Oslo (Mm ³ /yr)		Abstractions SWEQ (2003 to 2019) (Mm ³ /yr)			Abstractions Oslo Agreement (Mm ³ /yr)		
	Israel	Palestinian	Israel	Palestinian	Israel	Palestinian	Total	Israel	Palestinian	Total
Western	602		350 - 360		160	20	180	300 - 400	5 - 10	305 - 410
Northern	87		140 - 150		48	42	90	100 - 110	45	145 - 155
Eastern	368		150		195	20	215	40	42	95
Total	1057		640 - 660		402	82	485	440 - 550	92 - 97	532 - 647

Table 1.1: Groundwater conditions from SWEQ and the Oslo B Agreement. Adapted from Bastiaanssen et al., 2022.

Water quality is also a problem in the region due to untreated sewage or waste and over-pumping. As a result of the over-pumping, brackish water is also found in some parts of the aquifer, which means that further uncontrolled exploitation can lead to groundwater salinization (El-Fadel et al., 2001; Harpaz et al., 2001).

2 | Literature Review

2.1 | Evapotranspiration in Water Management

Evapotranspiration (ET) is defined as the combination of two processes in which water is lost: transpiration from the plants, which can be seen as water absorption from the root zone, and evaporation from the soil

surface, or water surface (R. Allen et al., 2002; Bogawski & Bednorz, 2014; Nolz, 2016). The hydraulics characteristics of the soil, the vegetation type and density, the precipitation, and water availability are factors that directly influence the ET and have a high spatial variability, making the ET highly variable in space. ET also has high variability in time due to the different weather and climate conditions (R. Allen et al., 2002; R. G. Allen et al., 2011).

Actual Evapotranspiration (ETA) is the primary consumer of liquid water in the hydrological cycle, and is, for that reason, considered one of the most important components of this system (R. G. Allen et al., 2011). ET has the capacity of controlling the availability and distribution of water at the Earth's surface when combined with rainfall and runoff (R. Allen et al., 1998; McCabe & Wood, 2006). To evaluate the water balance and water-use efficiency a water accounting is done, and for that, ET is the most important water flux (Karimi et al., 2013).

There are many different land uses in a river basin, such as irrigated and rainfed agriculture, forests, wetlands, and native and riparian vegetation, and in all of them evapotranspiration is responsible for transmitting water into the atmosphere. According to the Food and Agriculture Organization of the United Nations (FAO), agriculture is responsible for 70% of the world's water consumption, and, in agriculture, most of the water consumption occurs through evapotranspiration. The high consumption of water by irrigation makes ET essential not only for irrigation management but also for drought monitoring, estimation of water storage in an area, and efficient water management. (Barideh & Nasimi, 2022). Also, approximately 60% of the averaged precipitation will end up in ET from the land surface. (Z.-L. Li et al., 2009).

Alongside with precipitation, ET is a good representation of the region's climate and can be used as a decision-supporting tool for water management, as it contributes to the surface energy balance. Therefore, maps and understanding of the actual evapotranspiration are important tools in addressing the issue of consumptive water use, as they can be used as a base for evaluating how the water is being used and how can trade-offs be applied when it comes to water allocation (Bastiaanssen et al., 2005).

Due to the great role of ET in the hydrologic water balance, especially in arid and semi-arid areas, any small error in the ET values can lead to a significant change in surface water flow (R. G. Allen et al., 2011; Bouwer et al., 2008). Thus, having reliable ET estimates can be very useful for irrigation planning, water regulation, river basin studies, and any area involving the research and efficient use and management of water resources, as it can be used as a good indication of irrigation effectiveness and total water consumption from vegetation (R. Allen et al., 2002; R. Allen et al., 1998; McCabe & Wood, 2006). Efficient water resources management will depend on the accurate estimation of evapotranspiration and how it changes according to the land use, precipitation, and climate. Evaporation estimation for an entire catchment is necessary for a good assessment of requirements for irrigation in water-scarce regions (Bouwer et al., 2008).

2.1.1 | Reference Evapotranspiration

Actual evapotranspiration (ETA) is a key element within the water balance framework, finding extensive application across various disciplines. However, in many cases, it is also necessary to find the reference evapotranspiration (ETref), which offers an estimation of the atmospheric evaporative demand (Z. Li et al., 2012).

In the 1970s, the concept of reference evapotranspiration (ET) emerged as a practical and well-defined replacement for potential ET. It serves as a measure of local weather conditions and represents the evapotranspiration from a specified vegetated surface. Reference ET acts as an evaporative index that enables engineers, hydrologists, water managers, and other professionals to estimate ET for various vegetation and surface conditions by utilizing "crop" coefficients, particularly in agricultural or landscaped areas. Over the past decade, there has been a trend toward standardization for convenience and reproducibility. The reference surface is now described as a hypothetical surface with specific characteristics. It is defined as the ET rate from a uniform surface of dense, actively growing vegetation with predetermined height and surface resistance. This vegetation should not experience water shortage and should cover an area of at least 100 meters, consisting of the same or similar vegetation. The ASCE Penman-Monteith (ASCE-PM) equation from ASCE Manual 70 represents these standardized surfaces, specifically for clipped, cool-season grass and alfalfa, which fall into the categories of short and tall surfaces, respectively (R. G. Allen et al., 2005).

2.2 | Remote sensing for ET data and water balance

The conventional methods to measure ET are based on field scales, such as the Bowen ratio, Eddy covariance method, and soil water balance. However, the measurement of temporal and spatial patterns of ET depends on a variety of factors, such as vegetation, soil types and water content variations, topography, weather, and climate (Bouwer et al., 2008). The most precise approach for estimating ET on the field involves using lysimeter

measurements. However, lysimeter measurements are relatively challenging, costly, and require significant amounts of time (Bogawski & Bednorz, 2014; Xu et al., 2012). Thus, as land surfaces are heterogeneous and water vapor transport processes are dynamic, field-based measurements are ineffective in estimating spatially distributed ET on a larger spatial scale. (Bezerra et al., 2015; Gao et al., 2008). For instance, automatic weather stations are not equipped to measure ET directly. Rather, they provide measurements of the state conditions of the lower atmospheric boundary layer, which can be used to estimate a reference ET. This reference ET is the amount of water that would be lost by a hypothetical green landscape that is always adequately watered (Bastiaanssen et al., 2022).

Measuring the patchiness of landscapes on the ground is challenging, but satellite remote sensing can detect these variations across a wide range of scales, even up to continental scales, and with spatial coverage that cannot be achieved through ground-based measurements. Although retrieving accurate data from satellite observations can be difficult, it is currently the only feasible approach for measuring relatively small-scale variations in surface fluxes and states at regional scales. Moreover, satellite observations can examine the same region at multiple scales using different sensors with various spatial, spectral, and temporal characteristics (McCabe & Wood, 2006).

The integration of remote sensing and geographic information systems (GIS) - both geospatial techniques - with ground-based data has been increasingly utilized in the development of new tools for water-use assessment and reporting, including water accounting, as it doesn't need much ground data to provide ET estimation for wide land surface areas (Al-Bakri et al., 2022; R. Allen et al., 2002). However, ET is a parameter that frequently necessitates further processing of spectral data and its direct measurement via satellite images is not possible (Karimi & Bastiaanssen, 2015). Consequently, remote sensing is an indirect technique for measuring ET, which involves applying a series of equations to convert the spectral radiances recorded by satellites into estimates of actual ET. The capability to indirectly measure basic ET processes from satellites has revolutionized our capacity for managing water resources (Bastiaanssen & Bos, 1999; Bastiaanssen et al., 2005; Dominique et al., 2005; Menenti, 2000).

As a result, several remote sensing methods have been developed to map actual evapotranspiration (ETa) with minimal ground data inputs, being possible to estimate the parameter even in regions where there is no prior information available regarding soil or crop conditions or field management practices (Bastiaanssen et al., 2005). These methods include surface energy balance models, reflectance-based basal crop coefficient methods, and RS-based FAO-56 Penman-Monteith (FAO56PM) direct approaches (R. G. Allen et al., 2007; Anderson et al., 2011; Bastiaanssen et al., 2012; Bastiaanssen et al., 1998).

Surface energy balance models estimate ET based on the surface radiation fields, estimating through latent heat flux a direct assessment of actual ET using semi-empirical remote sensing approaches such as SEBAL (Surface Energy Balance Algorithm for Land) and its variant METRIC (Mapping Evapotranspiration at High Resolution with Internalized Calibration), and M-SEBAL (Modified Surface Energy Balance Algorithm for Land), beyond S-SEBI (Simplified Surface Energy Balance) (Bezerra et al., 2015; Gebremichael et al., 2010).

These models are based on the surface energy balance equation, which explains how natural radiation absorbed at Earth's surface is divided among various land surface processes. Evapotranspiration is a critical process in the energy balance since evaporation necessitates the consumption of latent heat (energy). The energy balance at Earth's surface can be seen below (Karimi & Bastiaanssen, 2015).

$$\lambda E = R_n - G - H \quad (\text{W m}^2) \quad (2.1)$$

λE is the latent heat flux, R_n is the net radiation, G is the soil heat flux, and H is the sensible heat flux.

The latent heat flux (λE) represents the amount of energy (measured in W/m^2) required to drive the ET flux, which is typically measured in units of $\text{kg/m}^2 \cdot \text{s}$ or mm/d . In this balance, shortwave solar radiation is the most critical source of energy and the net radiation absorbed at the land surface is determined by calculating the exchanges of shortwave and long-wave radiation. The sensible heat flux (H) is influenced by the temperature gradient between the canopy surface and the lower atmosphere, while the soil heat flux (G) is similarly influenced by the temperature difference between the land surface and the topsoil. While an increase in surface temperature will typically lead to an increase in H and G fluxes, evaporative cooling will lead to a reduction in H and G fluxes, which will lead to a reduction in surface temperature.

To measure the surface temperature, which is the most important input variable in ET algorithms, spaceborne radiometers like the Advanced Very High-Resolution Radiometer (AVHRR), Moderate Resolution Imaging Spectrometer (MODIS), Visible Infrared Imager Radiometer Suite (VIIRS), Landsat, Advanced Spaceborne Thermal Emission and Reflection Radiometer (ASTER), China-Brazil Earth Resources Satellite (CBERS), and the Chinese HJ and Feng Yung satellites are routinely used (Karimi & Bastiaanssen, 2015).

Various models provide different thermal infrared ET algorithms with variations that are typically linked to the parameterization of H , underlying model assumptions, and the quantity of input data necessary to run

them. According to Karimi and Bastiaanssen, 2015 several ET algorithms are based on the vegetation index and its derivatives. The ETLook model, which is more recent, directly calculates the surface energy balance by utilizing surface soil moisture estimates. These estimates can be obtained using either thermal or microwave measurements. Microwave measurements can provide a solution for all types of weather conditions and can be applied to any spatial scale where moisture data is available (Bastiaanssen et al., 2012).

One of the most common points of criticism in remote sensing data is the lack of accuracy, which has been improved in the last 30 years (Karimi & Bastiaanssen, 2015). As most energy balance models that are used to estimate ET use remotely sensed surface temperature as a key boundary condition, the pixel resolution for this data is very important for an accurate result (KUSTAS & NORMAN, 1996). When the model is used in crop fields, for instance, the individual fields usually have a length scale that is smaller than the pixel resolution of the surface temperature data that is available from satellites. As a result, the pixels will contain multiple different types of crops or land use, leading to a model that can not discriminate the field condition and, consequently, estimates an ET with significant errors (W. P. Kustas & Norman, 2000; W. Kustas et al., 2004). The Land Remote Sensing Satellite (Landsat) is one instrument that provides remotely sensed surface temperature data at pixel resolutions below 100 m. However, the infrequency of repeated coverage (every 16 days) and the possibility of cloud cover make it difficult to establish a routine application (W. Kustas et al., 2004). Despite some difficulties, Karimi and Bastiaanssen, 2015 analysis on the accuracy of remote sensing to estimate ET proves that the science has advanced and the mapping of ET has become more reliable.

This paper will explain further the surface energy balance model SEBAL, which was used for the ET estimate in the present study, and the RS-based FAO-56 Penman-Monteith (FAO56PM) approach used on the WaPOR model, which was used to estimate ET in the previous report by Bastiaanssen et al., 2022 made to do the water accounting in the Mountain Aquifer in Israel and Palestine.

2.2.1 | Google Earth Engine

Google Earth Engine (GEE) has gained major attention when it comes to remote sensing big data processing. It is a cloud-based platform that takes the power of Google's cloud infrastructure to enable parallelized processing of geospatial data on a global scale. One of the main advantage of GEE is that it offers free access to a big amount of remotely-sensed data in over 40 years. This includes datasets such as Landsat, MODIS, NOAA AVHRR, Sentinel 1, 2, 3, and 5-P, as well as ALOS data (Gorelick et al., 2017).

GEE provides an innovative platform for conducting geo-big data analyses in various environmental applications. It has many advantages such as its computational capabilities, good free satellite imagery availability, and scripting tools. These special and unique features made GEE superior to its competitors and the first choice for many researchers. However, there are some limitations. One is the limited availability of algorithms for object-based image analysis and clustering methods within GEE (Tamiminia et al., 2020).

2.2.2 | SEBAL (Surface Energy Balance Algorithms for Land) model

SEBAL model is the tool chosen to estimate the ET in this study. The SEBAL method employs satellite sensor-recorded spectral radiance and meteorological data to resolve the energy balance at the land surface, making it possible to estimate the actual ET on a pixel-by-pixel spatial level. The daily ET is calculated from the instantaneous latent heat flux (LE) at the time of satellite overpass (Bezerra et al., 2015).

The main approach of SEBAL is the method to estimate the sensible heat flux (H) which entails a complex procedure incorporating micrometeorological concepts to compute parameters for atmospheric stability corrections and aerodynamic resistance (R. G. Allen et al., 2007; Bastiaanssen, 2000; Gebremichael et al., 2010).

As explained before, SEBAL is a model that performs the surface energy balance at the satellite overpass time. Therefore, it uses the surface energy balance equation 2.1 to obtain the latent heat flux λE (W/m^2). The first step is to calculate net radiation (R_n), and, for that, some steps are necessary to obtain spectral radiance, reflectivity, albedo, emissivity, and land surface temperature. The second step is to compute the soil heat flux (G), which is determined using a semi-empirical approach that takes into account the NDVI, surface temperature, and albedo. The sensitive heat flux (H) is then computed by utilizing wind speed observations, estimated surface roughness, and surface-to-air temperature differences. To correct for atmospheric instability caused by buoyancy effects of surface heating, SEBAL employs an iterative process relating air density (ρ_{air}), specific heat of air at constant pressure (C_p) and near-surface temperature difference (dT), which is estimated as a linear function of the corrected surface temperature, to the aerodynamic resistance (ra_h), which is determined iteratively using Monin-Obukhov similarity theory until a stable value is reached. This value is used to calculate the near-surface temperature difference (dT) at the hot pixel, where the ET is assumed to be zero. The

temperature difference (dT) at the cold pixel is also calculated, and the relationship between the two is used to derive the temperature difference (dT) and, consequently, the sensible heat flux (H) for all pixels in the image.

The process of choosing "hot" and "cold" pixels is essential for the quality of the ET computation. Those are two "anchor" pixels, located in the area of interest of the study, chosen to fix boundary conditions for the energy balance. The "cold" pixel is designated as a moist, well-irrigated crop surface with complete ground coverage by vegetation. At this pixel, it is assumed that the surface temperature and near-surface air temperature are comparable. On the other hand, the "hot" pixel is identified as a parched, uncovered agricultural field where evapotranspiration (ET) is assumed to be absent. These two "anchor" pixels should be located in expansive and uniform areas that encompass more than one band 6 pixels. More explanation about the process of choosing the "hot" and "cold" pixels and the detailed processes of the SEBAL model can be found in R. Allen et al., 2002; Bastiaanssen et al., 2005; Bezerra et al., 2015; Jaafar and Mourad, 2021; Karimi and Bastiaanssen, 2015.

After calculating the latent heat flux (λE) for each pixel, SEBAL computes the equivalent instantaneous ET (mm/hr) by dividing λE by the latent heat of vaporization (λ). These values are then extrapolated to obtain daily or seasonal levels of ET using a ratio of ET to reference crop ET. The reference crop ET, known as E_{Tr} , is the expected ET rate from a defined surface of full-cover alfalfa or clipped grass and is computed in the SEBAL process using ground weather data (R. Allen et al., 2002; Bezerra et al., 2015).

The SEBAL method uses medium-resolution Landsat data for irrigation and hydrological applications and is widely employed. According to Bastiaanssen et al., 2005, these are SEBAL's applications: "(1) the relationship between land use and water use for river basin planning; (2) studying the impact of water conservation projects on real water savings; (3) irrigation performance; (4) environmental impact assessment due to groundwater extractions; (5) assessing the effect of water transfer design; (6) water-rights compliance; (7) hydrological modeling; (8) monitoring the degradation of native vegetation systems; (9) forest vitality; and (10) assessing crop water productivity, to name a few applications". However, it can be prone to bias in ET estimates. To mitigate this, ground data are often incorporated (Al-Bakri et al., 2022).

The SEBAL method has demonstrated its greatest success when applied to large, uniform irrigated areas located in arid and semi-arid climates, where it is more likely that the assumptions regarding evaporation from wet and dry pixels are valid (Bastiaanssen et al., 1998). In order to evaluate the accuracy of the SEBAL method, many field methods in which measurements are taken to determine the evaporative fluxes and partition available radiant energy into sensible and latent heat fluxes were already used. Inspections of the results under different conditions were made to validate the accuracy of the mode, using catchment-scale water balances that are as "known" as possible (Bastiaanssen et al., 2005).

According to Bastiaanssen et al., 2005 SEBAL has been proven to meet the requirements for an ideal ET information source, such as providing spatially detailed data that enable analysis at the field, project, and catchment levels, covering extensive areas such as entire river basins, and accounting for non-pristine growing conditions. SEBAL has been proven to meet these requirements for its ET estimates.

An analysis of SEBAL results for different studies, made by Bastiaanssen et al., 2005, showed that SEBAL's accuracy in estimating ET for single-day events and at a scale of around 100 ha is within $\pm 15\%$. The accuracy can be improved through space and time integration. Seasonal differences are relatively smaller (1 to 5%) due to the reduction in the random error component. For catchment scale studies, the overall deviation is 4% on an annual basis. All the testing of SEBAL made in the last decade, considering different climates and ecosystems, showed that the model is effective in solving water resource and irrigation-related issues. Javadian et al., 2019 also analyzed different studies that applied SEBAL for the estimation of ET and concluded that SEBAL has a good performance with different satellites and works well for the purpose of estimating water budget.

2.2.3 | FAO's WAPOR product

The Food and Agricultural Organization of the United Nations (FAO) has developed a portal to facilitate the monitoring of water productivity in Africa and the Middle East using remotely-sensed data (WaPOR) that is available to the public. One of the datasets offered on this portal is the Actual Evapotranspiration and Interception (ETIa), which is calculated utilizing the ETLOOK algorithm (Bastiaanssen et al., 2012). The FRAME Consortium, led by eLEAF and composed of the Flemish Institute for Technological Research (VITO), the International Institute for Geo-Information Science and Earth Observation at the University of Twente, and the WaterWatch Foundation, are responsible for producing the WaPOR datasets. The data is filled in and smoothed to eliminate any gaps, ensuring that all products are complete (Blatchford et al., 2020).

From April 2009 to now, ETIa has been provided on a 10-day, monthly, and annual basis at three different levels. The first level is the continental level (250 m), which covers the entire Africa and the Middle East region. The second level is the national level (100 m), which includes 21 countries and 4 river basins. The third level (30 m) encompasses eight irrigation areas, in Egypt, Ethiopia (2 areas), Mali, Lebanon, Kenya, Mozambique,

and Sudan. (Blatchford et al., 2020; FAO, 2020) Also, the WaPOR portal utilizes seasonal phenology data from the crop calendar and 10-day reflectance time series to perform Land Cover Classification (LCC) (Barideh & Nasimi, 2022).

To calculate ETIa on the WaPOR portal, it is necessary to have daily precipitation data. This is obtained through the use of CHIRPS (Climate Hazards Group InfraRed Precipitation with Station), an external data source that blends satellite observations with global models, with approximately 5 km pixel size, and on-site measurements from local stations (Barideh & Nasimi, 2022). According to Prakash, 2019, CHIRPS is a dependable dataset suitable for long-term analysis.

The FAO56PM method is often favored over other methods because of its ability to separate ET components into evaporation and transpiration and was developed to generate the free data of ET and water productivity through the FAO's WaPOR. This separation gives the necessary data for assessing the beneficially used fraction of irrigation water, which is an important indicator of water use efficiency. This method enables the acquisition of monthly Actual Evapotranspiration (ET) values directly for each pixel without using any groundwater-related information. Knowledge of monthly ET values on a 250 m grid provides valuable insights into local hydrological processes, especially in cases where ET exceeds precipitation, providing strategic information on local water excess. When precipitation (P) exceeds ET, there must be runoff or recharge, whereas when ET exceeds P, there must be a non-rainfall source of water resources. Therefore, the ET grids can be used as P-ET to describe local water management conditions. It is worth noting that the WaPOR technology can also be implemented on a 10 m, 30 m, or 100 m grid, making it possible to obtain unparalleled spatial precision in determining water consumption by crops, forests, and natural ecosystems (Bastiaanssen et al., 2022).

In countries where water scarcity is a challenge, the utilization of WaPOR datasets to monitor and develop water resources holds significant importance (Al-Bakri et al., 2022). The accuracy of the WaPOR was analyzed in many previous studies, According to Blatchford et al., 2020, the dataset on actual evapotranspiration and interception was of sufficient quality to enable understanding and monitoring of regional and continental water management and related processes. Rahimpour, 2021 reached the conclusion that the actual evapotranspiration and interception dataset for FAO's WaPOR had acceptable levels of accuracy when compared to the observed data, by calculating the mean absolute error (MAE), root mean square error (RMSE), and correlation (R). Also, When comparing the temporal and spatial scales, the maps generated by the WaPOR were deemed more realistic than the METRIC estimate (which was derived from MODIS images). This may be attributed to the ETLook algorithm's capacity to compute ET using microwave images even in cloudy conditions (Javadian et al., 2019).

2.3 | Previous studies in the Mountain Aquifer basin

This study uses as a main source the latest water accounting study made by Bastiaanssen et al., 2022. However, other studies with previous results are also taken into consideration to make a better analysis of our results and better understand the hydrological processes in the study area.

The previous report made by Bastiaanssen et al., 2022 using FAO's WaPOR database concluded that most of the actual ET values vary from 100 to 1100 mm/year in the area of interest of this study. In 2.1 it is possible to see the spatial distribution of ET across the Mountain Aquifer. While mountainous forests with high rainfall may have an ET rate of 800 mm or more, high ET values in most other areas can be attributed to the availability of water supplies. Lakes, the Dead Sea, irrigated crops, and groundwater-dependent ecosystems, for example, all have high ET values.

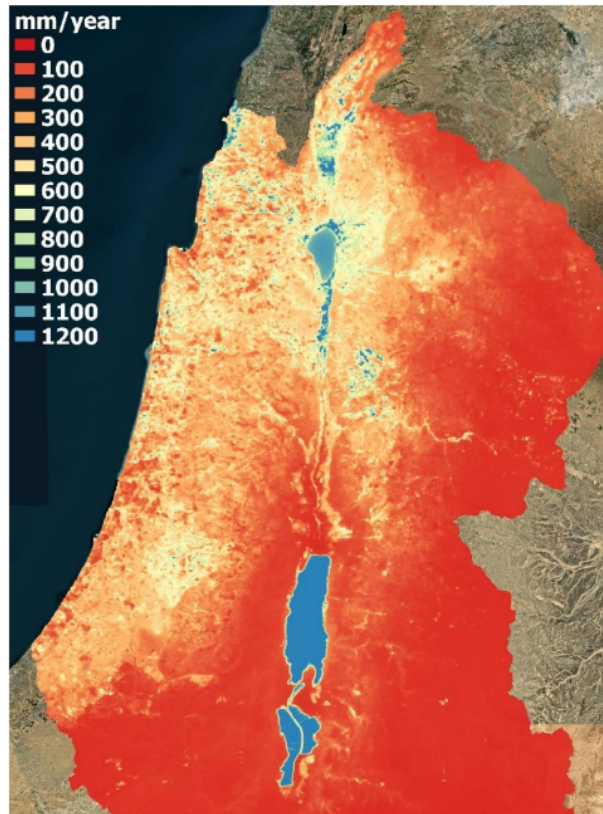


Figure 2.1: Spatial variability of longer term actual evapotranspiration (2003 to 2019) computed with the pyWaPOR version of the ETLook model (Bastiaanssen et al., 2022)

The climate in the region is Mediterranean, with moderate wet winters and dry warm summers. The primary source of the aquifer's water renewal is the precipitation in the mountains. The area has annual rainfall varying a lot throughout the years, but mainly from over 600 mm in the mountains, between 300-600 mm along the western foothills, and between 100-270 on the Jordan Rift Valley. Springs on the western foothill and on the valleys in the region serve as the natural outlets of the groundwater (Harpaz et al., 2001). Haddad, 1990 shows that the yearly potential evapotranspiration is typically higher than the mean yearly precipitation, as can be seen in Table 2.1. Nonetheless, infrequent intense rainfall events manage to seep into the aquifer and are then stored for future human usage. Consequently, the Mountain Aquifer is of significant strategic value to both parties in the area due to the prevailing arid conditions.

Region	Annual Rainfall (mm)	Annual Evapotranspiration (mm)	Daily Temperature (°C)	Annual Temperature Range (°C)
Coastal Plain	400 to 600	1700	19	13 to 26
Mountains	500 to 700	1850	17	8.5 to 22
Jordan Valley	50 to 150	2300	23	11 to 40

Table 2.1: Precipitation, Evaporation and Temperatures in the Mountain Aquifer

Bastiaanssen et al., 2022 found the following values for precipitation, evapotranspiration, and outflow discharge, respectively, for the Jordan River basin for the period 2003 to 2019: 248 mm/yr, 242 mm/yr, and 6 mm/yr.

Some conclusions can be made by analyzing the results for P - ET in the study area, seen in Figure 2.2. The North watershed boundaries exhibit high values of P-ET, resulting in the majority of renewable water resources in the study area. Additionally, the Westbank generates a significant amount of water resources due to P exceeding ET, particularly in areas with sparse vegetation and low ET. Notably, urban areas also act as water producers because their low ET is caused by the presence of buildings, roads, and pavements. In Figure 2.2, areas, where ET is greater than P, are highlighted in red, indicating that additional water is required through streams, pipelines, canals, aquifers, or interflow. As water flows from areas with P greater than ET to areas with ET greater than P, Figure 2.2 possibly indicates lateral water movements in the study area.

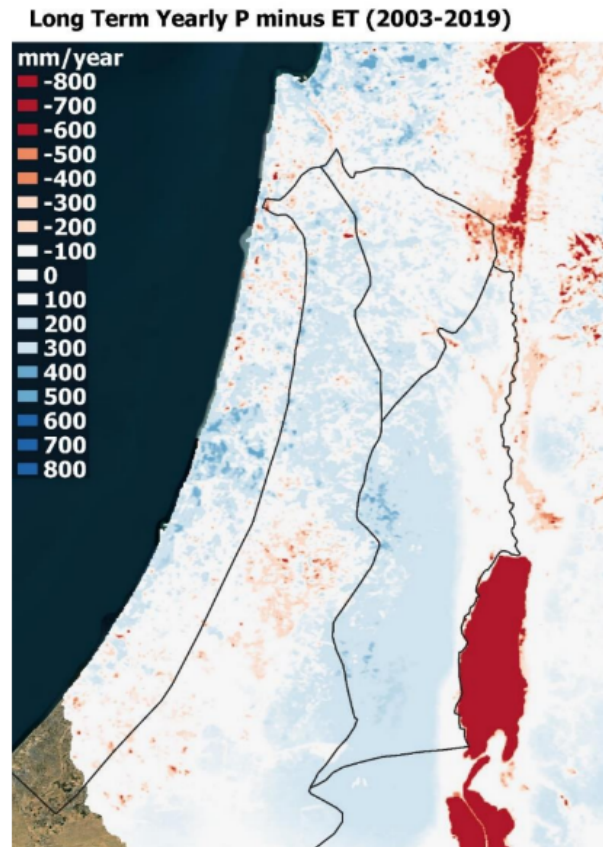


Figure 2.2: Spatial variation of areas producing water ($P > ET$) and areas that are net consumers ($P < ET$) (Bastiaanssen et al., 2022)

Sheffer et al., 2010 calculated the mean annual potential evaporation over the Western Mountain Aquifer, with precipitation varying from 1400 to 1800 mm. The mean annual actual ET is estimated to be 65%–75% of annual precipitation (Gvirtzman, 2002; Sheffer et al., 2010). Dweik et al., 2017 calculated the ET in the West Bank in the eastern aquifer basin, in Palestine territory. Using a spatial modelling approach to evaluate and estimate the water budget for the 50-year period (1950–2000), ET was calculated by a modified FAO Penman-Monteith equation. As a result, it was found that the evapotranspiration was varying from 500 to 700 mm/year for historic Palestine and from 500–620 mm/year for the eastern aquifer area.

Jebreen et al., 2018 calculated the actual ET for the Central Western Catchment, using water balance models. The approach utilizes a monthly time step, using data collected from sampling sites. The findings indicated that the annual evapotranspiration in the study area follows a pronounced topographic pattern with coves, valleys and the west-facing slopes having low rates of ET, while higher rates were found on ridges and especially on slopes with easterly aspects. Also, in the east part of the Central Western Catchment, it was found higher annual ET values when comparing to the west, due to its higher elevation. The values found for annual actual ET vary from 403 to 380 mm.

Helman et al., 2015 averaged the fluxes of precipitation (P), and discharge (Q) and calculated ET from six catchments along the north-south rainfall gradient in the eastern Mediterranean over the years 2000–2013 and the result can be seen in Table 2.2. MA-N, MA-CS, and MA-S stand for the northern, central-southern, and southern parts of the Mountain Aquifer of Israel, respectively. These are in situ ET values obtained by measured precipitation and discharge for that period.

Land use maps were obtained from Palestinian authorities by Bastiaanssen et al., 2022, and Table 2.3 shows water utilization in the region by land cover. In several forests, the annual ET ranges from 700 to 1000 mm/yr, indicating their dependence on groundwater unless surface irrigation is practiced. The continuous ET during prolonged periods without P is the primary evidence for this dependence. Furthermore, forests may intercept excess water from upstream micro-catchments in higher elevations.

According to Table 2.3, crops are the region's main groundwater user. Therefore, studies regarding ET from irrigated crops are very important for this analysis. During the summer of 2007, in a 45 days period, Rozenstein et al., 2019 conducted ET measurements in a commercial cotton field situated near Negba in the Shfela region of Israel. The results showed that irrigated crops in the area have a typical ET value in a range of 600 to 1000

Name	Area (10 ³ ha)	P (mm)	Q (mm)	ET (mm)
Kziv	13	799	284	515
HaShofet	1.2	654	183	471
MA-N	59	615	183	471
MA-CS	93	592	193	422
MA-S	28	619	202	362
Mamashit	6	130	28	102

Table 2.2: Precipitation (P), discharge (Q) and evapotranspiration (ET) from six catchments along the north-south rainfall gradient in the eastern Mediterranean (Helman et al., 2015)

	Crops (%)	Forest and bush (%)	Pastures (%)	Urban (%)	Total (%)
Israel	49.7	27.0	7.0	16.3	100.0
Palestinian Territories	42.2	10.5	18.4	29.0	100.0

Table 2.3: Groundwater abstraction by land use

mm/yr. The crop coefficient (Kc) value obtained in the study also showed it went from 0.9 at the beginning of summer to 0.4 by the end of the measurements. The average ET for the summer was calculated considering the average Reference ET of 180 mm, with a value of 200 mm for August and 160 mm for September, and the Kc of 0.65. The result showed an ET of 3.9 mm/d, which means 702 mm/yr in the case of the 180 days cycle for growing cotton, and the result matches the values for irrigated crops according to the WaPOR portal.

Another ET study was made by Rosa et al., 2013 on tomato crops, in a 14 days measurement period, in August, which is the growing season. The method used was the surface reveal with calibration against eddy covariance fluxes. The results showed a monthly ET of 171 mm, for a reference ET of 200 mm and Kc of 0.86.

An ET study was made by Bhantana and Lazarovitch, 2010 in Negev Israel, using lysimeters on pomegranates fields for 240 days and had, as a result, actual ET for pomegranates of 544 and 577 mm/ season, depending on the different variations of the crop. The annual ET values were estimated to be around 600 mm, and 200 mm under saline conditions, which coincides with the values from Bastiaanssen et al., 2022 that show the average ET values for cropland located in Southern Israel, which typically range from 200 to 600 mm/yr. However, these values are comparatively lower than those observed in Northern Israel and the Jordan Valley of Kfar Blum.

3 | Methodology

3.1 | SEBAL algorithm

SEBAL uses thermal and multispectral remote sensing datasets to estimate the latent heat (LE) consumed by the ET process. This is done by calculating the residual of the instantaneous surface energy balance equation (2.1). Equations 3.1 and 3.2 represent the net radiation (Rn) and the soil heat flux (G), respectively.

$$Rn = (1 - \alpha)Rs \downarrow + Rl \downarrow - Rl \uparrow - (1 - \epsilon_0)Rl \downarrow \tag{3.1}$$

$$\frac{G}{Rn} = \alpha(T_s - 273.15)(0.0038\alpha + 0.0074\alpha^2)(1 - 0.98NDVI^4) \tag{3.2}$$

For:

$$T_s = \frac{K_2}{\ln\left[\frac{\epsilon_{nb}K_1}{L_t} + 1\right]} \tag{3.3}$$

Where:

- α is the surface albedo
- $Rs\downarrow$ is the incoming shortwave radiation
- $Rl\downarrow$ is the incoming longwave radiation
- $Rl\uparrow$ is the outgoing longwave radiation

- ϵ_0 is the surface thermal emissivity
- K_1 and K_2 are constants obtained from image properties for each Landsat product
- ϵ_{nb} is the narrow band emissivity
- L_t is the corrected thermal radiance from the surface

Albedo (α) is calculated using a weighted combination of different bands in a satellite image, which in this case, is using the Landsat 8 surface reflectance bands. Surface thermal emissivity (ϵ_0) is calculated based on the Normalized Difference Vegetation Index (NDVI). Shortwave incoming radiation is determined by multiplying the atmospheric transmittance with the instantaneous extraterrestrial solar radiation. The atmospheric emissivity is then calculated using the Bastiaanssen et al., 1998 formula. Instantaneous incoming longwave radiation is computed using the atmospheric emissivity, Stefan-Boltzmann constant, and temperature in Kelvin. Similarly, instantaneous outgoing longwave radiation is calculated using the surface thermal emissivity and surface temperature.

To calculate T_s , preprocessing, temperature calculation, and thermal sharpening techniques were used to derive a higher-resolution surface temperature from the original thermal band (T) by incorporating information from the Fractional Vegetation Cover (FV). Next, surface temperature (T_s) was standardized to a uniform elevation reference point (T_{sdem}) through the integration of digital elevation data from the Shuttle Radar Topography Mission (SRTM), factoring in an average lapse rate of 6.5 °C km. Additionally, any slope-related effects were remedied. The corrected T_s (T_{scorr}) can be found by Equation 3.4 (Jaafar & Ahmad, 2019).

$$T_{scorr} = T_{sdem} + \frac{[G_{sc}^* d_r^* \tau_{sw}^* (\cos\theta_{slope} - \cos\theta_{flat})]}{1004\rho_0.05} \quad (3.4)$$

Where:

- G_{sc} is the solar constant
- d_r is the inverse-relative distance Earth-Sun
- τ_{sw} is the atmospheric transmissivity
- θ_{slope} is the solar incidence angle for slope terrain
- θ_{flat} is the solar incidence angle for flat terrain
- ρ_a is the air density

To calculate the sensible heat flux (H) an iterative process is necessary because on Equation 3.5, there are two unknowns, H and (r_{ah}).

$$H = \frac{\rho_a C_p dT}{r_{ah}} \quad (3.5)$$

Where:

- r_{ah} is the aerodynamic resistance to turbulent heat transport
- C_p is the specific heat capacity

A JavaScript code that selects cold and hot endmembers was used to solve the iterative process above. The cold pixel function calculates cold pixels based on negative NDVI values and low land surface temperature values. It identifies the top 5% of pixels with the lowest NDVI and further selects the lowest 20% of land surface temperature values within those pixels. It calculates the median T_s and the sum of cold pixels. The hot pixel function identifies hot pixels based on positive NDVI values and high land surface temperature values. It follows a similar process to the cold pixels but selects the top 10% of NDVI values and the top 20% of T_s values. It calculates the median T_s , the sum of hot pixels.

The near-surface temperature difference (dT) needs to be defined for each pixel in order to compute H and solve the iteration process. Therefore, a linear relationship between T_s and dT is assumed in Equation 3.6. The coefficients "a" and "b" are correlation coefficients and determined through empirical methods for each individual image.

$$dT = a + bT_s \quad (3.6)$$

The sensible heat flux (H) is estimated using the previously calculated hot pixel's temperature, NDVI, and other variables. It involves iterative calculations to determine the aerodynamic resistance and temperature difference between hot and cold pixels. In the wet (cold) condition, λE corresponds to all available energy, and H is assumed to be zero. λE_{cold} is assumed to be $1.05 ET_r$ and then H_{cold} can be calculated with 2.1. Once you have H_{cold} , you can calculate dT_{cold} with Equation 3.7. However, in the dry (hot) condition, H is assumed to be at its maximum and λE is assumed to be zero. Therefore, the same process takes place, using 2.1 and 3.7, but on hot pixels, to find H_{hot} and dT_{hot} .

$$dT_{cold} = \frac{H_{cold} r_{ah,cold}}{\rho_{cold} C_p} \quad (3.7)$$

Initially, r_{ah} is estimated using Equation 3.8, and in each iteration, an atmospheric stability correction is applied based on the Monin-Obukhov similarity (Bastiaanssen et al., 1998) until a stable value is obtained.

$$r_{ah} = \frac{\ln \frac{z_1}{z_2}}{k u^*} \quad (3.8)$$

Where:

- z_1 and z_2 are the starting and ending evaporating surface height on the turbulent heat transport
- u^* is the friction velocity, estimated by Equation 3.9
- k is the von Karman constant

For u^* found by Equation 3.9

$$u^* = \frac{u_{200} k}{\ln \frac{200}{z_{om}}} \quad (3.9)$$

Where:

- z_{om} is the surface roughness
- u_{200} is the wind speed at a blending height of 200

Now that the latent heat was found (LE) it is possible to calculate the evaporative fraction (Λ), which represents the ratio of latent heat flux to net radiation, through Equation 3.10. Λ is restricted to values between 0 and 1.6 to ensure physical plausibility.

$$\Lambda = \frac{LE}{R_n - G} \quad (3.10)$$

Λ is then used to finally calculate the daily ET. The advection factor (AF) accounts for the effect of advection on evapotranspiration and is computed based on Λ , the saturation vapor pressure and the actual vapor pressure. The daily evapotranspiration (ETA) is calculated by Equation 3.11.

$$ET_{24h} = \frac{\Lambda AF (R_{n24h} - Refl_w)}{(\lambda 1000) 86400000} \quad (3.11)$$

Where:

- R_{n24h} is the net radiation daily average
- $Refl_w$ is the reflected radiation at water surface

R_{n24h} and $Refl_w$ are calculated by Equation 3.12 and 3.13, respectively.

$$R_{n24h} = R_{ns24h} - R_{nlFAO} \quad (3.12)$$

$$Refl_w = R_{n24h} G_{w24h} \quad (3.13)$$

Where R_{ns24h} is the net shortwave radiation calculated by multiplying the 24-hour radiation by $(1 - \alpha)$. R_{nlFAO} is the net outgoing radiation found using the FAO equation, which requires the temperature in Kelvin,

Stefan-Boltzmann constant, actual vapor pressure, and transmissivity. G_{w24h} is the solar radiation received at the water surface in a 24-hour period, being assigned ad 0.1, representing the albedo for water.

Finally, a threshold is defined. The crop coefficient (Kcb) is calculated using the image's normalized difference vegetation index (NDVI). Kcb is adjusted based on the slope of the pixel. If the slope is above a certain threshold, Kcb is multiplied by 1.1. Finally, the calculated ET_{24h} is compared to a threshold value based on the slope. If ET_{24h} exceeds threshold, ET_{24h} is replaced with threshold value.

3.2 | FAO's WaPOR product

The primary mechanism of ETLook involves a thermal evaluation of soil moisture in the root zone, where colder land surfaces are presumed to contain more moisture. By combining this information with data on Leaf Area Index and weather conditions from climatic models, the actual fluxes of soil evaporation (E) and vegetation transpiration (T) are calculated using a 2-layer Penman-Monteith model (Bastiaanssen et al., 2022)

ETia is estimated using the ETLook algorithm with some modifications in the Penman-Monteith equation, which is a method that combines the energy balance and aerodynamic equations by utilizing remote sensing data such as NDVI, surface albedo, soil moisture, solar radiation, ground cover, and digital elevation model (DEM) and meteorological data, such as precipitation, temperature, wind speed and humidity (FAO, 2020). These modified equations incorporate vegetation cover information based on the ETLook model, allowing for differentiation in net available radiation and resistance formulas. The WAPOR approach estimates soil moisture using land surface temperature (Blatchford et al., 2020).

Figure 3.1 illustrates the main concepts of the WaPOR product, solving two parallel Penman-Monteith equations. In this scheme, you can see that transpiration is coupled with the soil through the subsoil or root zone soil moisture content. On the other hand, evaporation is coupled with the soil through the soil moisture content of the topsoil. Interception refers to the process in which leaves intercept rainfall and evaporate directly from the leaves, utilizing energy that is not accessible for transpiration.

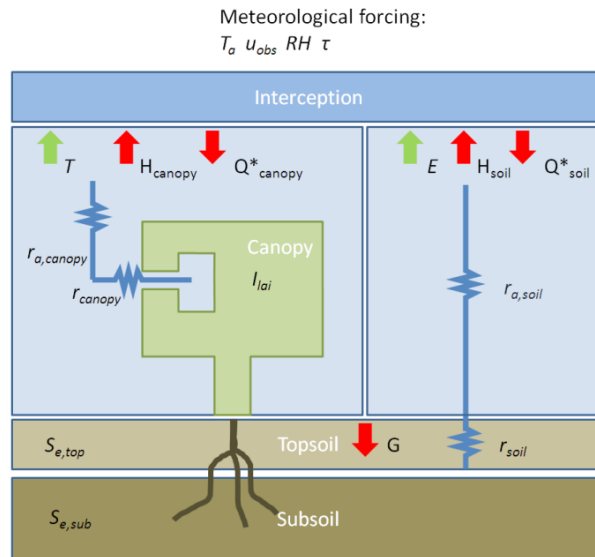


Figure 3.1: WaPOR model main concepts scheme (FAO, 2020)

Thus, the ET Look model uses this method to estimate evaporation and transpiration separately, using a daily time step and equations 3.14 and 3.15. Then, the evaporation and transpiration are combined with the interception, which is a function of the vegetation cover, leaf area index (LAI), and precipitation, as can be seen in Equation 3.16, to calculate the ETia (Bastiaanssen et al., 2012; Blatchford et al., 2020).

$$\lambda E = \frac{\Delta(R_{n,soil} - G) + p \left(\frac{\Delta e}{r_{a,soil}} \right)}{\Delta + \gamma \left(1 + \frac{r_{soil}}{r_{a,soil}} \right)} \quad (3.14)$$

$$\lambda T = \frac{\Delta(R_{n,Canopy}) + p \left(\frac{\Delta e}{r_{a,Canopy}} \right)}{\Delta + \gamma \left(1 + \frac{r_{Canopy}}{r_{a,Canopy}} \right)} \quad (3.15)$$

$$\lambda I = 0.2LAI \left(1 - \frac{1}{1 + \frac{F_c P}{0.2LAI}} \right) \quad (3.16)$$

Where:

- λ is the latent heat of evaporation
- $\Delta = d(e_{sat})/dT$ is the slope of the saturation vapor pressure
- γ is the psychometric constant
- ρ is the density of air
- C_p is the specific heat of air
- Δ_e is the vapor pressure deficit
- r_a is the aerodynamic resistance
- r_s is the soil resistance or canopy
- F_c is the vegetation cover calculated from NDVI
- LAI is the leaf area index

$R_{n,soil}$ is the net radiation from the soil and canopy. They can be found by Equations 3.17 and 3.18.

$$R_{n,soil} = [(1 - \alpha_0)R \downarrow - L_n - I] \exp(-aLAI) \quad (3.17)$$

$$R_{n,canopy} = [(1 - \alpha_0)R \downarrow - L_n - I][1 - \exp(-aLAI)] \quad (3.18)$$

Where:

- α_0 is surface albedo
- $R \downarrow$ is the incoming shortwave radiation
- γ is the psychometric constant
- L_n is the net longwave radiation
- a is the light extinction coefficient for the net radiation

The soil heat flux for the WaPOR product can be found in Equation 3.19.

$$G = \frac{\sqrt{2}A_{t,year}k \sin\left(\frac{2}{p} - \frac{\pi}{4}\right)}{z_d} \exp(-aLAI) \quad (3.19)$$

Where:

- $A_{t,year}$ is the yearly temperature amplitude
- k is the soil thermal conductivity
- J and p is the day of the year and number of days in the year respectively
- z_s is the damping depth

The aerodynamic resistance can be found under neutral conditions or under non-neutral conditions. Equations 3.20 and 3.21 represent the aerodynamic resistance for non-neutral conditions.

$$r_{a,soil} = \frac{\ln \frac{z_{obs}-d}{0.1z_{om,soil}} - \Psi_{h,obs}}{k u_*} \quad (3.20)$$

$$r_{a,canopy} = \frac{\ln \frac{z_{obs}-d}{0.1z_{om,canopy}} - \Psi_{h,obs}}{k u_*} \quad (3.21)$$

Where:

- k is the von Karman constant
- u_* is the friction velocity
- d is the displacement height
- $z_{om,soil}$ and $z_{om,canopy}$ is the soil/canopy surface roughness
- $\Phi_{h,obs}$ is the stability correction for heat

A detailed explanation of the ETLook model can be found in (Bastiaanssen et al., 2012)

3.2.1 | WaPOR vs Sebal model

In order to facilitate the comparison between the results by the WaPOR product and the SEBAL model, 3.1 and 3.2 were made.

Table 3.1: Equations used in WaPOR and SEBAL

Equation	WaPOR	SEBAL
λE	$\lambda E = \frac{\Delta(R_{n,soil} - G) + p \left(\frac{\Delta \epsilon}{r_{a,soil}} \right)}{\Delta + \gamma \left(1 + \frac{r_{soil}}{r_{a,soil}} \right)}$	$\lambda E = R_n - G - H$
Rn	$R_{n,soil} = [(1 - \alpha_0)R \downarrow - L_n - I] \exp(-aLAI)$ $R_{n,canopy} = [(1 - \alpha_0)R \downarrow - L_n - I][1 - \exp(-aLAI)]$	$Rn = (1 - \alpha)Rs \downarrow + Rl \downarrow - Rl \uparrow - (1 - \epsilon_0)Rl \downarrow$
G	$\frac{G}{Rn} = \alpha(T_s - 273.15)(0.0038\alpha + 0.0074\alpha^2)(1 - 0.98NDVI^4)$	$G = \frac{\sqrt{2}A_{t,year} k \sin\left(\frac{2\pi J}{p} - \frac{\pi}{4}\right)}{z_d} \exp(-aLAI)$
r_{ah}	$r_{a,soil} = \frac{\ln \frac{z_{obs} - d}{0.1z_{om,soil}} - \Psi_{h,obs}}{\frac{ku_*}{z_{obs} - d}}$ $r_{a,canopy} = \frac{\ln \frac{z_{obs} - d}{0.1z_{om,canopy}} - \Psi_{h,obs}}{ku_*}$	$r_{ah} = \frac{\ln \frac{z_1}{z_2}}{ku^*}$

Table 3.2: Main differences between WaPOR and SEBAL

Product	Remote sensing data input	Meteorological data	Calculations	Advantage
SEBAL	NDVI, albedo, surface temperature, emissivity and daily incoming shortwave radiation	Surface temperature, wind speed, air temperature, surface solar radiation, dewpoint temperature, and total precipitation	Instantaneous ET flux	Higher resolution, few model input parameters and wide application range
WaPOR	NDVI, surface albedo, soil moisture, solar radiation, Land use cover and digital elevation model (DEM)	Air temperature, precipitation, humidity, and wind speed	Evaporation, transpiration, and interception separately	Application in larger areas, applicable in any weather condition and taking into account humidity and soil

3.3 | Google Earth engine application

3.3.1 | Preparing and preprocessing the Landsat

To use the SEBAL model on GEE, some steps must be taken to prepare the Landsat images as a preprocessing step for geospatial data analysis. The image collection employed for this study comprises imported data from Landsat 5, 7, and 8 satellites, encompassing both tier 1 and tier 2 datasets. These image collections offer a comprehensive selection of current and historical images at 30 x 30 meters spatial resolution. By utilizing these datasets, the aim is to estimate the evapotranspiration (ET) time series spanning from 2003 to 2021.

Furthermore, the study area was delineated as the Mountain Aquifer, ensuring that the generated data pertains specifically to this region.

After importing the image collections, the image has to be prepared and preprocessed, filtering out cloudy pixels. It also calculates the area's local time and time zone. The first part of the code defines variables to extract latitude and longitude information from the region of interest (ROI). It then calculates the difference between the local time and Greenwich Mean Time, the Local Standard Time Meridian, and the rounded difference between the local time and Greenwich. These variables are used later when importing Landsat data. The second part of the code defines a function that takes in several arguments, including Landsat image collections (Landsat 5, 7, and 8), the ROI, start and end dates, and offset GTM (which is the rounded difference between the local time and Greenwich).

Functions that are designed to filter and mask clouds within Landsat data are incorporated. These functions are utilized to process the Landsat images, where the filtered images are subsequently sorted chronologically and merged together to form a unified image for each specific date. The resulting image collection comprises cloud-free Landsat images. The functions are versatile and accommodate various versions of Landsat sensors while ensuring consistent mapping of spectral bands to standardized names. The masking process involves eliminating clouds and cloud shadows based on the Quality Assessment (QA) band, filling in gaps in the Landsat imagery using a focal mean filter, and removing images that lack valid pixels. Additionally, several preprocessing steps are implemented, including the selection of a Digital Elevation Model (DEM) that is clipped to the region of interest (ROI). This step is crucial in considering the solar incidence angle for slope analysis and accounting for flat terrain when applying the T_s correction. Furthermore, the Landsat 5, 7, and 8 datasets are combined into a single collection, and the necessary bands required for image processing are prepared.

3.3.2 | Obtaining meteorological data

The GEE platform offers access to the complete Landsat collection and hourly ERA5 Land data. The choice of ERA5 Land was primarily based on its extensive global coverage and superior spatial and temporal resolution compared to other reanalysis data accessible in GEE. Table 3.3 shows all datasets used in the code and their time coverage and resolution, respectively.

Table 3.3: Time coverage and resolution of the datasets from GEE platform that were used in this study

Product	Time coverage	Resolution - Visible and infrared bands	Resolution - Thermal bands
LANDSAT 8 OLI/TIRS	Apr/2013 - Present	30 m	60 m
LANDSAT 7 ETM+	Jan/1999 - Present	30 m	100 m
LANDSAT 5 TM	Mar/1984 – May/2012	30 m	120 m
ERA5-Land hourly	Jan/1981 – Present	0.1°	-
SRTM	One survey mission (Feb/2000)	30 m	-

This study employs a customized code implemented within the Google Earth Engine (GEE) platform to extract hourly weather data from the ERA5-Land dataset. These weather data are subsequently interpolated to align with the Landsat satellite overpass time, ensuring consistent and synchronized weather information is acquired concurrent with the Landsat satellite imagery. First, the code retrieves the ERA5-Land dataset for global meteorological inputs. It selects the required bands for surface pressure, air temperature at 2m (T_{air}), eastward and northward wind speed at 10m (u and v), surface solar radiation, dewpoint temperature (T_{dew}), and total precipitation. It then applies bi-cubic resampling to the ERA5-Land images and advances their system time by the offset time. Finally, the function maps over the Landsat image collection and interpolates the ERA5-Land data to the Landsat overpass time. The resulting image collection contains consistent weather data with the Landsat satellite images. A workflow of the model on GEE can be seen in Figure 3.2.

3.4 | Data processing

To facilitate a comprehensive comparison of our findings, it is imperative to calculate the annual values for Actual Evapotranspiration (ETA). Consequently, additional steps must be undertaken to obtain ETA measurements on a yearly basis and to determine the average ETA from the years 2003 to 2021, expressed in millimeters per year.

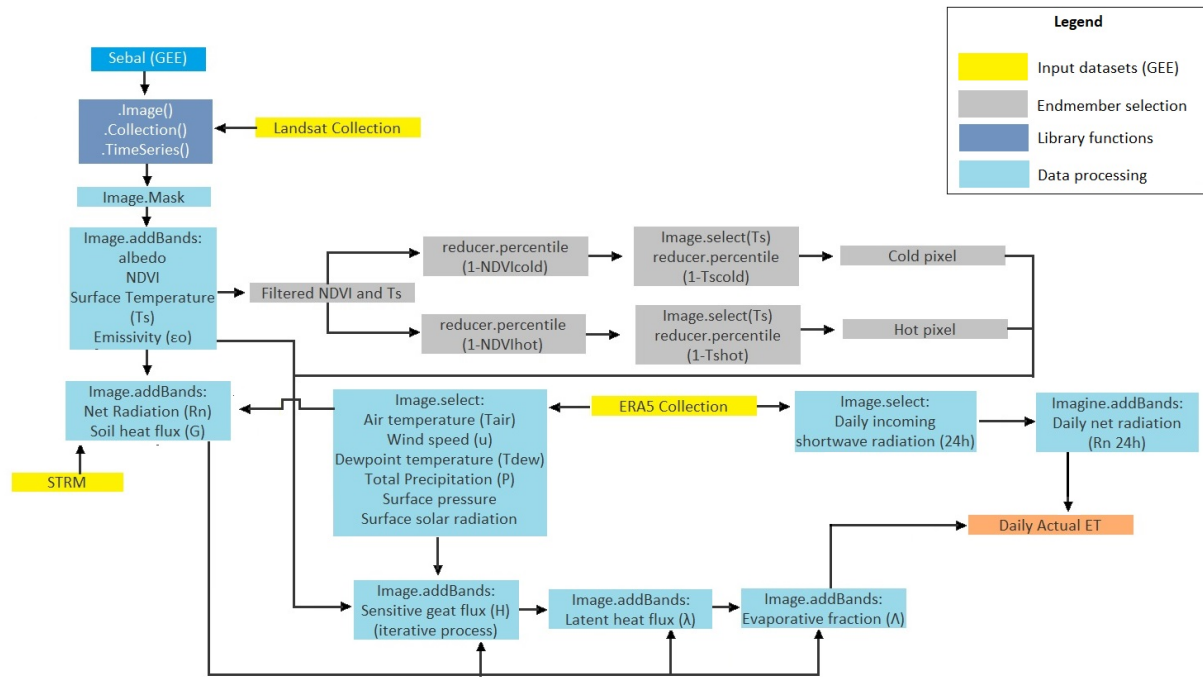


Figure 3.2: Workflow of Sebal model on GEE (Adapted from Laipelt et al., 2021)

3.4.1 | Generating annual ET_a data

Daily ET_a was generated from day-to-day ET output from the SEBAL model following the Equation 3.22.

$$ET_{daily} = ET_{ratio} \times ET_{ref} \quad (3.22)$$

where ET_{ratio} is the daily ET_{ratio} calculated as ET_a/ET_{ref} , and ET_{ref} is the reference evapotranspiration, and further explanation on ET_{ref} generation can be found in 6. Monthly ET_a is derived by cumulatively adding the daily ET_a for each month.

To facilitate a comprehensive analysis of the results, annual maps of ET_a were generated. Additionally, a TIFF file was created, to represent the average annual ET_a from 2003 to 2021. This single TIFF file provides an overview of the average ET_a value across all years, allowing for a broad assessment of the long-term ET_a patterns. These maps and average values provide valuable insights for further investigation and understanding of the ET_a patterns over the specified time period in the study area.

3.5 | Land use analysis

The land use in the basin plays a significant role in affecting the evapotranspiration (ET) and hydrological cycle. Understanding the land type is crucial for comparing ET levels. In this particular study, the Land use map of the Mountain Aquifer was employed to gain insights into various land uses and assess ET in different regions. For that purpose, it was used the European Space Agency (ESA) WorldCover 10 m 2020, which provides a land cover map for 2020 at 10 m resolution based on Sentinel-1 and Sentinel-2 data.

3.6 | Comparing datas

To compare the data produced by the SEBAL model with the existing data from the WaPOR product, the software ArcGIS was employed to quantify the disparity between their long-term average evapotranspiration (ET_a) values. The land use map was also utilized to gain insights into the variations between the two methods.

4 | Results and discussion

4.1 | Actual Evapotranspiration (ETa) results

The results of the analysis are presented in Table 4.1, which displays the calculated mean, maximum, minimum, and standard deviation values for both the yearly average ET_a and the Long Term average spanning from 2003

to 2021. Moreover, Figure 4.1 has been generated to visually illustrate the Long Term average ETA from 2003 to 2021. This image serves as a graphical representation of the average evapotranspiration pattern observed over the analyzed period. Overall, the ETa values vary until 2400 mm/year, with an average between 600 and 800 mm/year. The picture makes it possible to see the spatial distribution across the Mountain Aquifer.

Table 4.1: Summary Statistics for ET Values (2003-2021)

Year	Max	Min	Mean	Stdev
2003	1910.56	0	658.68	417.61
2004	2432.58	8.76	770.42	440.31
2005	2063.86	0.98	653.98	415.63
2006	1959.60	0.64	663.80	431.58
2007	1927.18	1.85	662.93	417.17
2008	2132.53	7.39	647.56	439.70
2009	2015.32	2.57	661.61	440.48
2010	2021.77	9.92	606.72	394.69
2011	2087.62	0	635.83	407.20
2012	2398.31	9.38	764.74	452.33
2013	2089.08	1.05	681.02	424.47
2014	2215.40	1.06	683.30	413.88
2015	1948.51	1.92	685.91	389.91
2016	2214.52	19.40	758.69	404.47
2017	2434.75	14.00	767.64	460.69
2018	2117.98	11.26	688.44	411.37
2019	2014.35	2.34	725.19	424.14
2020	1921.20	45.21	793.44	386.20
2021	2100.70	14.79	756.77	441.69
Long Term Average	1912.41	36.54	680.05	423.80

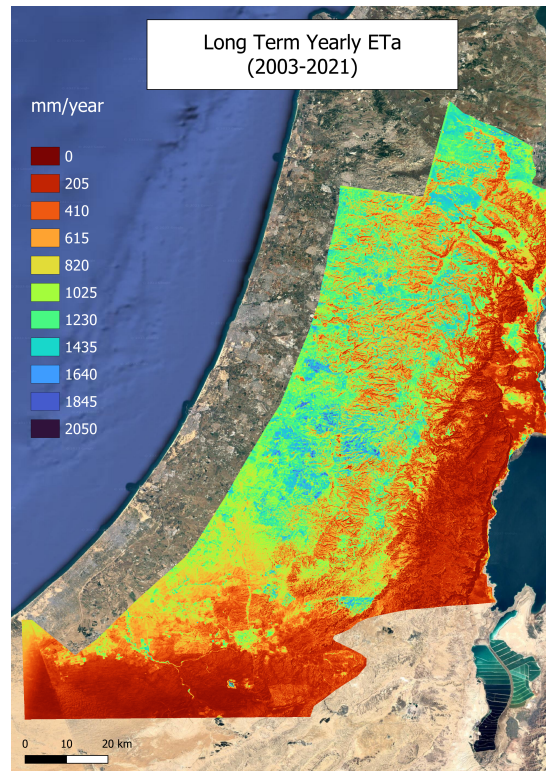


Figure 4.1: Long Term Yearly ETa (2003-2021)

4.1.1 | Land Use Analysis

The generation of a land use map for the area was undertaken to enhance the comprehension of the geography and landscape characteristics within the region, facilitating the interpretation of the ETa values obtained. Figure 4.2 displays the Land Use map, while Table 4.2 presents the corresponding percentages of each land use category observed in the region.

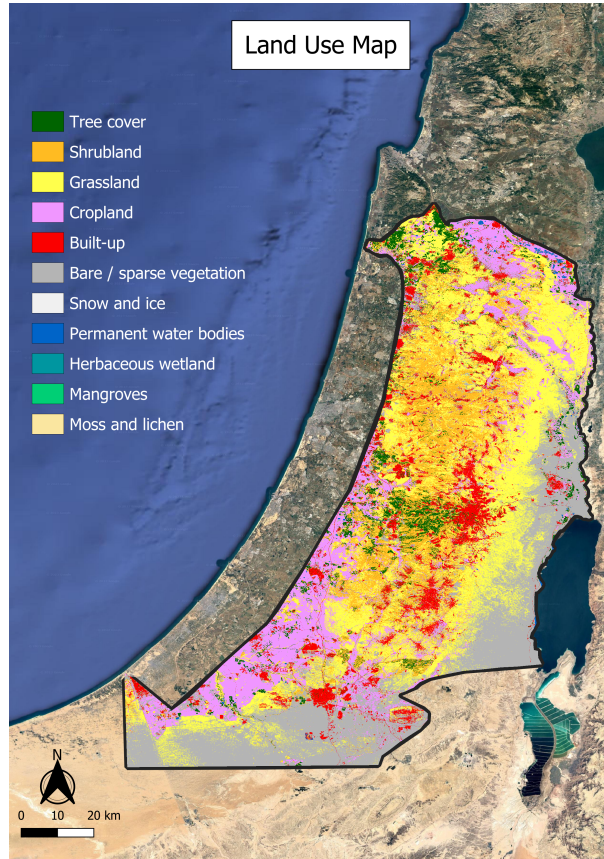


Figure 4.2

Table 4.2: Land Use (percentage)

Land use	Area (km ²)	Percentage (%)
Tree cover	526.71	4.94
Shrubland	1603.32	15.04
Grassland	3188.61	29.91
Cropland	1719.46	16.13
Urban area	889.67	8.35
Bare/sparse vegetation	2708.82	25.41
Permanent water bodies	21.50	0.20
Herbaceous wetland	1.55	0.01

Figure 4.3 was generated to compare the average ETa values among various Land Use types. The analysis reveals elevated ETa values are associated with accessible water resources, irrigated crop cultivation, and groundwater-dependent ecosystems, such as areas with dense tree cover.

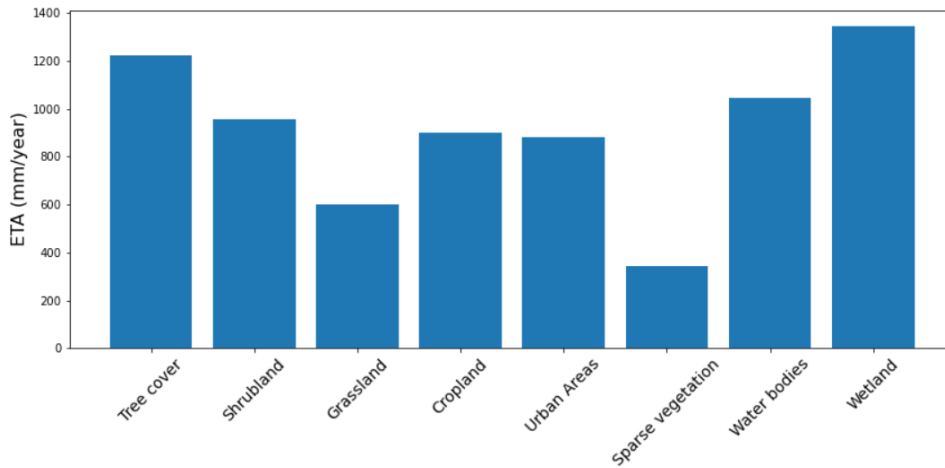


Figure 4.3: Mean ETa for different land use types

The SEBAL model is considered most accurate and reliable for computing evapotranspiration (ET) in flat, agricultural areas. When comparing the results for cropland areas with a study conducted by Rozenstein (2019) in the same region, the ETa values obtained in this study fall within the range of 600 to 1000 mm/year, as reported in their findings. This suggests that the ETa values derived using the SEBAL model align with the range of values reported in the aforementioned study.

4.1.2 | Comparative Analysis of ETa Results: SEBAL Model versus WAPOR Product

When comparing the findings of this study with the previous report (Bastiaanssen et al., 2022), disparities in the results become apparent. The difference between the two results was calculated for each pixel, generating a map representing the spatial distribution of the values found, as can be seen in Figure 4.5. Furthermore, Figure 4.4 presents a time series plot illustrating the mean ETa trends from 2003 to 2019 for both methods.

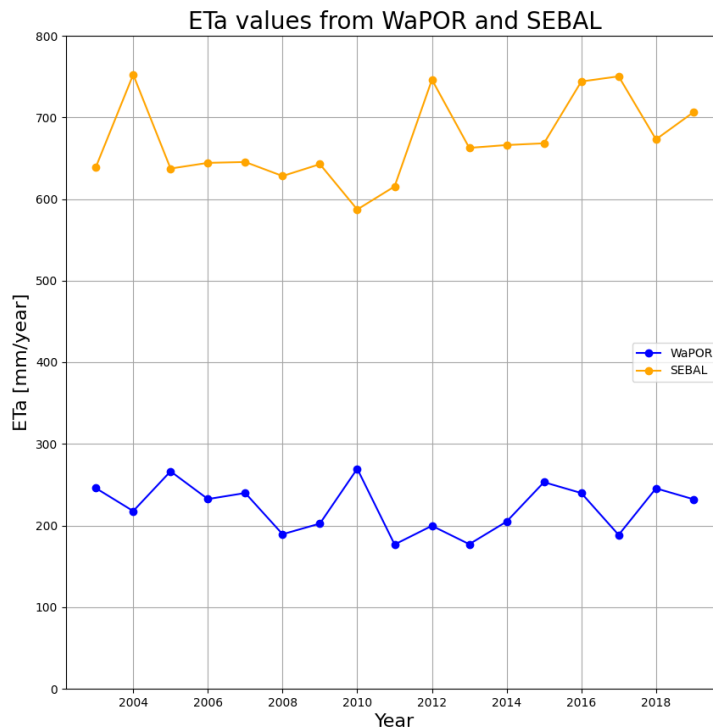


Figure 4.4: Mean ETa values from WaPOR and SEBAL

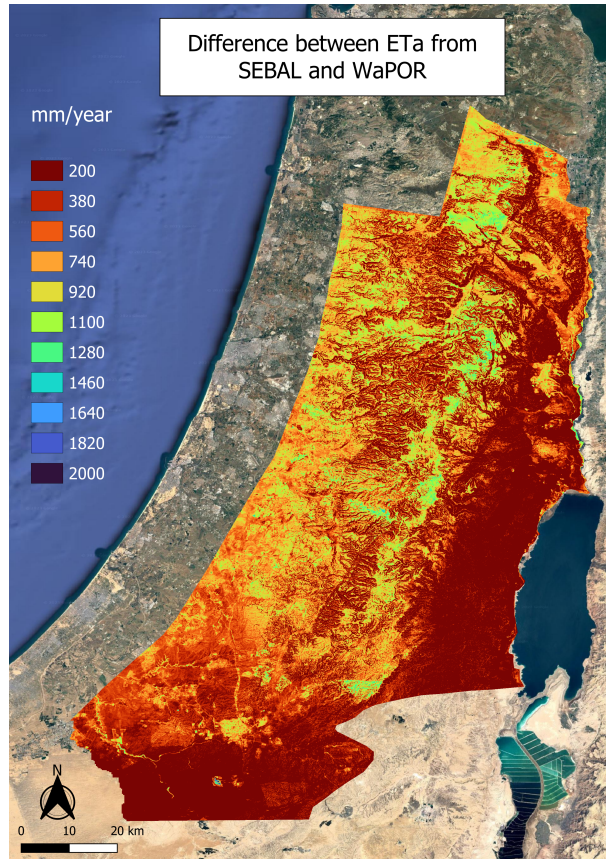


Figure 4.5

Table 4.3 provides a comparative analysis of the ETa values obtained in our study with those reported in previous studies conducted in the same region using different methodologies. The results demonstrate considerable variability among the studies, which can be attributed to variations in the adopted methods and spatial resolutions. However, it is noteworthy that the ETa value derived from our study falls within the average range reported by Dweik et al. (2017) and exhibits closer proximity to the findings of Sheffer et al. (2020). However, it is important to note that the findings of Sheffer et al. (2020) were made for the Mountain Aquifer, but not exactly to the same extent as the study, while Dweik et al. (2017) focused on the Eastern Aquifer Basin.

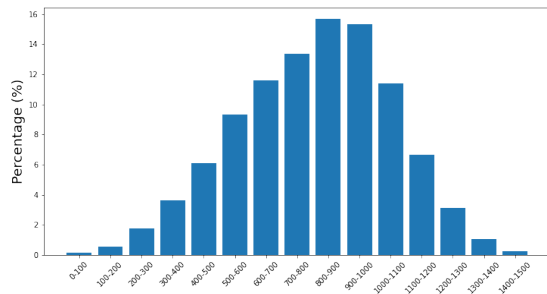
Table 4.3: ETa values from different studies

Current study	Bastiaanssen (2022)	Sheffer et al. (2020)	Dweik et al., 2017
SEBAL model	WaPOR	Daily Recharge Assessment Model (DREAM)	Spatial modelling approach (own model)
680 mm/yr	242 mm/yr	455-525 mm/yr	500-700 mm/yr

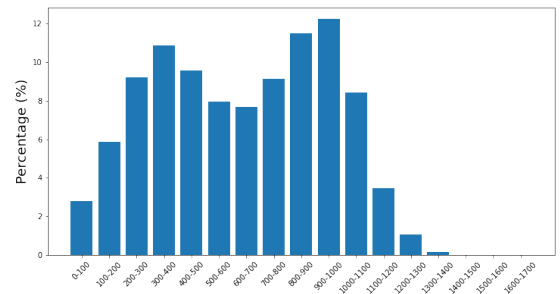
When compared to existing literature, the results from the WaPOR method tend to underestimate the values. Additionally, previous studies have indicated that the WaPOR product consistently underestimates observed values. At the same time, the Sebal algorithm tends to overestimate them, resulting in a substantial difference ranging from 3 to 6 mm/day (Javadian et al., 2019). This could potentially explain the notable differences observed in this study's findings.

To enhance the interpretation of the results presented in Figure 4.5, the data was extracted and categorized based on different land use types, utilizing the previously generated land use information. Subsequently, Figure 4.6 was created by focusing on the six predominant land use categories, displaying the maps depicting the difference between the two results for each category.

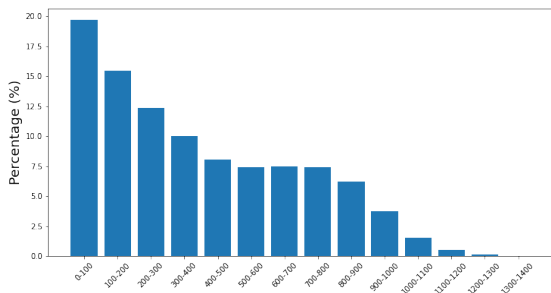
Observing the results, it becomes evident that grassland and sparse vegetation exhibit the smallest discrepancies between the utilized methods, whereas tree cover and urban areas display the most significant disparities.



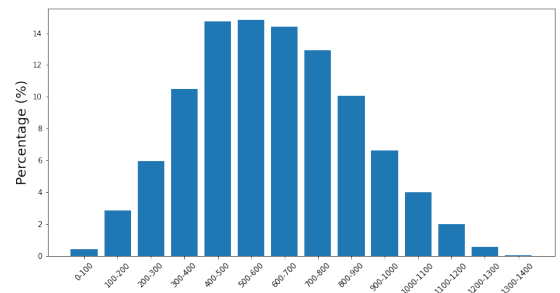
(a) Treecover



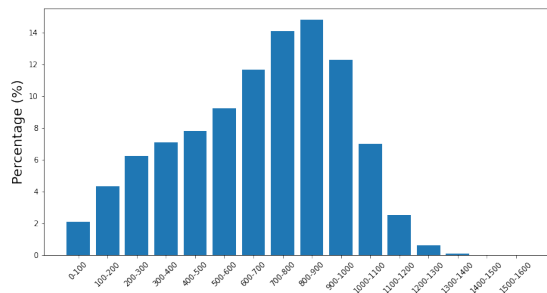
(b) Shrubland



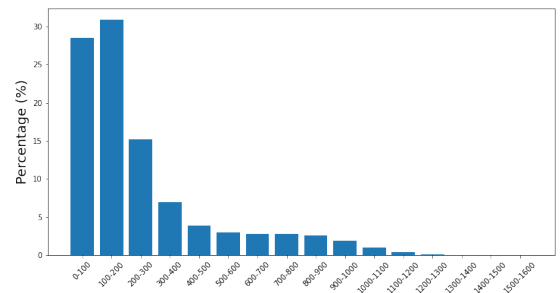
(c) Grassland



(d) Cropland



(e) Urban area



(f) Bare and sparse vegetation

Figure 4.6: Difference between ETA from the SEBAL model and WaPOR product, per land use type

The SEBAL model is not primarily designed for urban areas, which may affect its accuracy when applied to such land use types. In the case of tree covers, the observed discrepancies can be attributed to multiple factors. One significant factor is the utilization of a higher resolution in this study compared to previous research. The increased resolution enables better incorporation of evapotranspiration from tree cover, contributing to the observed differences. The research on developing accurate assessment methods for products derived from moderate to low spatial resolution data is still ongoing. Landscape characteristics, such as land cover heterogeneity and patch size, play a significant role in classification accuracy at coarser resolutions. As patch size decreases and heterogeneity increases, the probability of achieving a correct classification decreases (FAO, 2020)

Other potential factor contributing to the substantial differences across land use types is the parameter 'a' (light extinction coefficient for the net radiation) employed in the equations for net radiation in the WaPOR product. This factor can vary considerably among different land use categories, potentially posing a limitation for the WaPOR product, as it utilizes a single value for all land use types (Chukalla et al., 2022). The lack of consideration for such variations may contribute to the larger differences observed in the results between land use types.

4.2 | Limitations

This study encountered several limitations that should be acknowledged. Firstly, the lack of available literature reporting actual evapotranspiration (ETA) data specifically for the Mountain Aquifer posed a challenge in validating the generated results. The studies found don't comprehend the exact same area as this study, limiting the comparison. With limited studies for comparison, it was difficult to assess the accuracy and reliability of our findings, particularly in comparison to results obtained from the WaPOR product.

Secondly, the time constraints imposed on data generation using Google Earth Engine (GEE) restricted the study area to the Mountain Aquifer alone, excluding the broader Jordan River basin. Since GEE sets limits on the maximum amount of processing time allowed for a single computation, there are limitations on the amount of data that can be processed at a given time. This narrows the scope of the analysis. Optimizing the processing workflow and avoiding manually running the code for each set of data could possibly be done by implementing a loop or iteration within your code, so it is possible to automate the process and handle a certain quantity of data at a time before moving on to the next set.

Considering these limitations, it is recommended that future studies explore strategies to overcome these challenges. Efforts should be made to expand the available literature on ETA in the Mountain Aquifer, enabling a more robust validation of the generated data. Additionally, optimizing the code used in GEE could enhance efficiency and allow for a broader spatial analysis encompassing the entire Jordan River basin.

5 | Conclusion

The primary objective of this study was to generate accurate actual evapotranspiration (ETA) data for the Mountain Aquifer region. The aim was to contribute to water allocation studies and assist in making informed water management decisions. Previous water accounting was made using the FAO's WaPOR product to calculate ETA with a resolution of 250 m, and the aim of this study was to generate new ETA data using the SEBAL model in GEE, with a 30 m resolution. This study's analysis of evapotranspiration (ETA) values provided valuable insights into the studied region's water dynamics and land use characteristics. The results indicated significant spatial and temporal variations in ETA, with values ranging till 2400 mm/year and an average of 600-800 mm/year.

Comparisons with previous studies demonstrated the variability of ETA values, which can be attributed to different methodologies and spatial resolutions. However, the ETA values obtained in this study aligned with the average range reported by previous studies. In contrast, the comparison with the WaPOR product indicated higher discrepancies, with the SEBAL ETA being higher. The discrepancies observed in this study's findings can be attributed to the limitations of each method and the variations in parameter values across different land use types. The higher resolution employed in this study enabled better incorporation of evapotranspiration, contributing to the observed differences.

The analysis of land use types revealed that grassland and sparse vegetation exhibited smaller discrepancies between methods, while tree cover and urban areas displayed more significant disparities. The SEBAL model, not primarily designed for urban areas, may experience accuracy issues when applied to such land use types.

In conclusion, this study provides valuable insights into evapotranspiration's spatial and temporal dynamics and its relationship with land use characteristics in the studied region. Through the analysis of evapotranspiration from different land use types, a notable finding is a significant role played by certain land types, such as tree

cover, in groundwater consumption. This observation highlights the importance of considering tree cover in groundwater resource management and allocation planning. By recognizing the influence of land use types in groundwater consumption, policymakers, and water managers can make informed decisions to ensure the sustainable utilization and allocation of groundwater in the region. The findings also highlight the importance of considering methodological differences, spatial resolutions, and land use variations when comparing ETa values.

Recommendations for future studies would be to include the entire Jordan River Basin for a better understanding of the entire region and to complete the water accounting. Overall, this study contributes to a better understanding of water resource management in semi-arid/arid regions and provides a foundation for further research.

References

- Al-Bakri, J. T., D'Urso, G., Batchelor, C., Abukhalaf, M., Alobeiaat, A., Al-Khreisat, A., & Vallee, D. (2022). Remote sensing-based agricultural water accounting for the north Jordan valley. *Water*, *14*(8). <https://doi.org/10.3390/w14081198>
- Allen, R., Tasumi, M., & Trezza, R. (2002). Sebal (surface energy balance algorithms for land)-advanced training and user's manual-idaho implementation.
- Allen, R., Pereira, L., & Smith, M. (1998). *Crop evapotranspiration-guidelines for computing crop water requirements-fao irrigation and drainage paper 56* (Vol. 56).
- Allen, R. G., Pereira, L. S., Howell, T. A., & Jensen, M. E. (2011). Evapotranspiration information reporting: li. recommended documentation. *Agricultural Water Management*, *98*(6), 921–929. <https://doi.org/https://doi.org/10.1016/j.agwat.2010.12.016>
- Allen, R. G., Tasumi, M., & Trezza, R. (2007). Satellite based energy balance for mapping evapotranspiration with internalized calibration (metric). *Journal of Irrigation and Drainage Engineering*, *133*(4), 380–394.
- Allen, R. G., Walter, I. A., Elliott, R. L., Howell, T. A., Itenfisu, D., Jensen, M. E., & Snyder, R. L. (2005). *The asce standardized reference evapotranspiration equation*. American Society of Civil Engineers. <https://doi.org/10.1061/9780784408056>
- Anderson, M. C., Kustas, W. P., Norman, J. M., Hain, C. R., Mecikalski, J. R., Schultz, L., González-Dugo, M. P., Cammalleri, C., d'Urso, G., Pimstein, A., & Gao, F. (2011). Mapping daily evapotranspiration at field to continental scales using geostationary and polar orbiting satellite imagery. *Hydrology and Earth System Sciences*, *15*(1), 223–239. <https://doi.org/10.5194/hess-15-223-2011>
- Barideh, R., & Nasimi, F. (2022). Investigating the changes in agricultural land use and actual evapotranspiration of the urmia lake basin based on fao's wapor database. *Agricultural Water Management*, *264*, 107509. <https://doi.org/https://doi.org/10.1016/j.agwat.2022.107509>
- Bastiaanssen, W. (2000). Sebal-based sensible and latent heat fluxes in the irrigated gediz basin, turkey. *Journal of Hydrology*, *229*, 87–100. [https://doi.org/10.1016/S0022-1694\(99\)00202-4](https://doi.org/10.1016/S0022-1694(99)00202-4)
- Bastiaanssen, W., & Bos, M. (1999). Irrigation performance indicators based on remotely sensed data: A review of literature. *Irrigation and Drainage Systems*, *13*, 291–311. <https://doi.org/10.1023/A:1006355315251>
- Bastiaanssen, W., Cheema, E. M. J., Immerzeel, W., Miltenburg, I., & Pelgrum, H. (2012). Surface energy balance and actual evapotranspiration of the transboundary indus basin estimated from satellite measurements and the etlook model. *Water Resources Research*, *48*, W11512. <https://doi.org/10.1029/2011WR010482>
- Bastiaanssen, W., Hessels, T., & Davids, J. (2022). Water accounts of the mountain aquifer: Reporting period 2003 to 2019.
- Bastiaanssen, W., Menenti, M., Feddes, R., & Holtslag, A. (1998). A remote sensing surface energy balance algorithm for land (sebal). 1. formulation. *Journal of Hydrology*, *212-213*, 198–212. [https://doi.org/https://doi.org/10.1016/S0022-1694\(98\)00253-4](https://doi.org/https://doi.org/10.1016/S0022-1694(98)00253-4)
- Bastiaanssen, W., Noordman, E., Pelgrum, H., Davids, G., Thoreson, B., & Allen, R. (2005). Sebal model with remotely sensed data to improve water-resources management under actual field conditions. *Journal of Irrigation and Drainage Engineering*, *131*, 85–93. [https://doi.org/10.1061/\(ASCE\)0733-9437\(2005\)131:1\(85\)](https://doi.org/10.1061/(ASCE)0733-9437(2005)131:1(85))
- Bezerra, B., Silva, B., Santos, C., & Bezerra, J. (2015). Actual evapotranspiration estimation using remote sensing: Comparison of sebal and sseb approaches. *Advances in Remote Sensing*, *04*, 234–247. <https://doi.org/10.4236/ars.2015.43019>
- Bhantana, P., & Lazarovitch, N. (2010). Evapotranspiration, crop coefficient and growth of two young pomegranate (*punica granatum* l.) varieties under salt stress. *Agricultural Water Management*, *97*, 715–722. <https://doi.org/10.1016/j.agwat.2009.12.016>

- Blatchford, M., Mannaerts, C., Muchiri Njuki, S., Nouri, H., Zeng, Y., Pelgrum, H., Wonink, S., & Karimi, P. (2020). Evaluation of wapor v2 evapotranspiration products across africa. *Hydrological Processes*, 34. <https://doi.org/10.1002/hyp.13791>
- Bogawski, P., & Bednorz, E. (2014). Comparison and validation of selected evapotranspiration models for conditions in poland (central europe). *Water Resources Management*, 28. <https://doi.org/10.1007/s11269-014-0787-8>
- Bouwer, L. M., Biggs, T. W., & Aerts, J. C. J. H. (2008). Estimates of spatial variation in evaporation using satellite-derived surface temperature and a water balance model. *Hydrological Processes*, 22(5), 670–682. <https://doi.org/https://doi.org/10.1002/hyp.6636>
- Chukalla, A. D., Mul, M. L., van der Zaag, P., van Halsema, G., Mubaya, E., Muchanga, E., den Besten, N., & Karimi, P. (2022). A framework for irrigation performance assessment using wapor data: The case of a sugarcane estate in mozambique. *Hydrology and Earth System Sciences*, 26(10), 2759–2778. <https://doi.org/10.5194/hess-26-2759-2022>
- Dominique, C., Seguin, B., & Olioso, A. (2005). Review on estimation of evapotranspiration from remote sensing data: From empirical to numerical modeling approaches. *Irrigation and Drainage Systems*, 19, 223–249. <https://doi.org/10.1007/s10795-005-5186-0>
- Dweik, F., Rahil, M., & Salama, M. (2017). Evaluation and assessment of water budget in the eastern aquifer basin of the west bank, palestine. *International Journal of Global Environmental Issues*, 16, 17. <https://doi.org/10.1504/IJGENVI.2017.083427>
- El-Fadel, M., Quba'a, R., El-Hougeiri, N., Hashisho, Z., & Jamali, D. (2001). The israeli palestinian mountain aquifer: A case study in ground water conflict resolution. *Journal of Natural Resources and Life Sciences Education*, 30(1), 50–61. <https://doi.org/https://doi.org/10.2134/jnrlse.2001.0050>
- FAO. (2020). *Wapor database methodology*.
- French, A., Jacob, F., Anderson, M., Kustas, W., Timmermans, W., Gieske, A., Su, Z., Su, H., McCabe, M., Li, F., Prueger, J., & Brunsell, N. (2005). Surface energy fluxes with the advanced spaceborne thermal emission and reflection radiometer (aster) at the iowa 2002 smacex site (usa) [Scientific Results from ASTER]. *Remote Sensing of Environment*, 99(1), 55–65. <https://doi.org/https://doi.org/10.1016/j.rse.2005.05.015>
- Gao, Y., Long, D., & Li, Z.-L. (2008). Estimation of daily actual evapotranspiration from remotely sensed data under complex terrain over the upper chao river basin in north china. *International Journal of Remote Sensing*, 29(11), 3295–3315. <https://doi.org/10.1080/01431160701469073>
- Gebremichael, M., Wang, J., & Sammis, T. W. (2010). Dependence of remote sensing evapotranspiration algorithm on spatial resolution. *Atmospheric Research*, 96(4), 489–495. <https://doi.org/https://doi.org/10.1016/j.atmosres.2009.12.003>
- Gorelick, N., Hancher, M., Dixon, M., Ilyushchenko, S., Thau, D., & Moore, R. (2017). Google earth engine: Planetary-scale geospatial analysis for everyone. *Remote Sensing of Environment*, 202. <https://doi.org/10.1016/j.rse.2017.06.031>
- Gvirtzman, H. (2002). *Israel water resources, chapters in hydrology and environmental sciences, yad ben-zvi press, jerusalem*.
- Haddad, M. (1990). State of the environment in the occupied territories. *Conference on the management of the Environment in the Mediterranean*.
- Harpaz, Y., Haddad, M., & Arlosoroff, S. .-. (2001). Overview of the mountain aquifer a shared israeli-palestinian resource. https://doi.org/10.1007/978-94-010-0680-4_3
- Helman, D., Givati, A., & Lensky, I. M. (2015). Annual evapotranspiration retrieved from satellite vegetation indices for the eastern mediterranean at 250 m spatial resolution. *Atmospheric Chemistry and Physics*, 15(21), 12567–12579. <https://doi.org/10.5194/acp-15-12567-2015>
- Israel Water Authority, I. (2019). *The issue of water between israel and the palestinians. israel water*.
- Jaafar, H., & Ahmad, F. (2019). Time series trends of landsat-based et using automated calibration in metric and sebal: The bekaa valley, lebanon. *Remote Sensing of Environment*, 238. <https://doi.org/10.1016/j.rse.2018.12.033>
- Jaafar, H., & Mourad, R. (2021). Gymee: A global field-scale crop yield and et mapper in google earth engine based on landsat, weather, and soil data. *Remote Sensing*, 13(4). <https://doi.org/10.3390/rs13040773>
- Jackson, T. J. (1997). Soil moisture estimation using special satellite microwave/imager satellite data over a grassland region [Cited by: 104]. *Water Resources Research*, 33(6), 1475–1484. <https://doi.org/10.1029/97WR00661>
- Javadian, M., Behrangi, A., Gholizadeh, M., & Tajrishy, M. (2019). Metric and wapor estimates of evapotranspiration over the lake urmia basin: Comparative analysis and composite assessment. *Water*, 11, 1647. <https://doi.org/10.3390/w11081647>

- Jebreen, H., Wohnlich, S., Wisotzky, F., Banning, A., Hachenberg, A., & Ghanem, M. (2018). Recharge estimation in semi-arid karst catchments: Central west bank, palestine. *Grundwasser*, 23. <https://doi.org/10.1007/s00767-017-0376-x>
- Karimi, P., & Bastiaanssen, W. G. M. (2015). Spatial evapotranspiration, rainfall and land use data in water accounting ndash; part 1: Review of the accuracy of the remote sensing data. *Hydrology and Earth System Sciences*, 19(1), 507–532. <https://doi.org/10.5194/hess-19-507-2015>
- Karimi, P., Bastiaanssen, W. G. M., & Molden, D. (2013). Water accounting plus (wa+) ndash; a water accounting procedure for complex river basins based on satellite measurements. *Hydrology and Earth System Sciences*, 17(7), 2459–2472. <https://doi.org/10.5194/hess-17-2459-2013>
- KUSTAS, W. P., & NORMAN, J. M. (1996). Use of remote sensing for evapotranspiration monitoring over land surfaces. *Hydrological Sciences Journal*, 41(4), 495–516. <https://doi.org/10.1080/02626669609491522>
- Kustas, W. P., & Norman, J. M. (2000). Evaluating the effects of subpixel heterogeneity on pixel average fluxes. *Remote Sensing of Environment*, 74(3), 327–342. [https://doi.org/https://doi.org/10.1016/S0034-4257\(99\)00081-4](https://doi.org/https://doi.org/10.1016/S0034-4257(99)00081-4)
- Kustas, W., Li, F., Jackson, T., Prueger, J., MacPherson, J., & Wolde, M. (2004). Effects of remote sensing pixel resolution on modeled energy flux variability of croplands in iowa [2002 Soil Moisture Experiment (SMEX02)]. *Remote Sensing of Environment*, 92(4), 535–547. <https://doi.org/https://doi.org/10.1016/j.rse.2004.02.020>
- Laipelt, L., Henrike Bloedow Kayser, R., Santos Fleischmann, A., Ruhoff, A., Bastiaanssen, W., Erickson, T. A., & Melton, F. (2021). Long-term monitoring of evapotranspiration using the sebal algorithm and google earth engine cloud computing. *ISPRS Journal of Photogrammetry and Remote Sensing*, 178, 81–96. <https://doi.org/https://doi.org/10.1016/j.isprsjprs.2021.05.018>
- Li, Z.-L., Tang, R., Wan, Z., Bi, Y., Zhou, C., Tang, B., Yan, G., & Zhang, X. (2009). A review of current methodologies for regional evapotranspiration estimation from remotely sensed data. *Sensors*, 9(5), 3801–3853. <https://doi.org/10.3390/s90503801>
- Li, Z., Zheng, F., & Liu, W.-Z. (2012). Spatiotemporal characteristics of reference evapotranspiration during 1961–2009 and its projected changes during 2011–2099 on the loess plateau of china. *Agricultural and Forest Meteorology*, 154–155, 147–155. <https://doi.org/10.1016/j.agrformet.2011.10.019>
- Libiszewski, S. (1995). Water disputes in the jordan basin region and their role in the resolution of the arab-israeli conflict. *Center for Security Policy and Conflict Research, Zurich; Swiss Peace Foundation, Berne*. <http://www.fsk.ethz.ch/encop/13/en13.htm>
- McCabe, M. F., & Wood, E. F. (2006). Scale influences on the remote estimation of evapotranspiration using multiple satellite sensors. *Remote Sensing of Environment*, 105(4), 271–285. <https://doi.org/https://doi.org/10.1016/j.rse.2006.07.006>
- Menenti, M. (2000). Remote sensing in hydrology and water management. https://doi.org/10.1007/978-3-642-59583-7_17
- Nolz, R. (2016). A review on the quantification of soil water balance components as a basis for agricultural water management with a focus on weighing lysimeters and soil water sensors / ein überblick über die ermittlung von wasserhaushaltsgrößen als basis für die landeskulturelle wasserwirtschaft mit fokus auf lysimeter und bodenwassersensoren. *Die Bodenkultur: Journal of Land Management, Food and Environment*, 67. <https://doi.org/10.1515/boku-2016-0012>
- Prakash, S. (2019). Performance assessment of chirps, mswep, sm2rain-cci, and tmpa precipitation products across india. *Journal of Hydrology*, 571, 50–59. <https://doi.org/10.1016/j.jhydrol.2019.01.036>
- Rahimpour, M. (2021). Validation and calibration of fao's wapor product (actual evapotranspiration) in iran using in situ measurements.
- Rosa, R., Dicken, U., & Tanny, J. (2013). Estimating evapotranspiration from processing tomato using the surface renewal technique. *Biosystems Engineering*, 114, 406–413. <https://doi.org/10.1016/j.biosystemseng.2012.06.011>
- Rozenstein, O., Haymann, N., Kaplan, G., & Tanny, J. (2019). Validation of the cotton crop coefficient estimation model based on sentinel-2 imagery and eddy covariance measurements. *Agricultural Water Management*, 223, 105715. <https://doi.org/10.1016/j.agwat.2019.105715>
- Sheffer, N. A., Dafny, E., Gvirtzman, H., Navon, S., Frumkin, A., & Morin, E. (2010). Hydrometeorological daily recharge assessment model (dream) for the western mountain aquifer, israel: Model application and effects of temporal patterns. *Water Resources Research*, 46(5). <https://doi.org/https://doi.org/10.1029/2008WR007607>
- Tamiminia, H., Salehi, B., Mahdianpari, M., Quackenbush, L., Adeli, S., & Brisco, B. (2020). Google earth engine for geo-big data applications: A meta-analysis and systematic review. *ISPRS Journal of Photogrammetry and Remote Sensing*. <https://doi.org/10.1016/j.isprsjprs.2020.04.001>

Xu, J., Peng, S., Ding, J., Wei, Q., & Yu, Y. (2012). Evaluation and calibration of simple methods for daily reference evapotranspiration estimation in humid east china. *Archives of Agronomy and Soil Science*, 59, 1–14. <https://doi.org/10.1080/03650340.2012.683425>

6 | Appendix A: Reference Evapotranspiration

To calculate the reference evapotranspiration (ET_{ref}), a GEE-based implementation of the ASCE Standardized Reference Evapotranspiration Equations for computing daily reference ET was chosen, using ERA5-Land Hourly image collection.

The image was first filtered for the specific years of the study, and the six variables that are needed for computing ET_{ref} from the ERA5 were used, which are surface pressure, air temperature at 2m (T_{air}), eastward and northward wind speed at 10m (u and v), surface solar radiation, and dewpoint temperature (T_{dew}).

Several operations related to terrain and geographical data are also performed, with terrain-related products such as slope, aspect, and hillshade being computed by elevation data. The resulting elevation, latitude, and longitude images can be used for further analysis and calculations involving terrain and geographical information.

Air pressure is then calculated based on the elevation data. It uses the elevation image to compute the air pressure using Equation 6.1, taking into account the relationship between elevation and air pressure, considering the decrease in pressure with increasing elevation.

$$p_{air} = 101.3 \left[\frac{(293 - 0.0065 \text{elevation})}{293} \right]^{5.25} \quad (6.1)$$

A function to estimate ET_{ref} using ERA5 data is defined, taking as an input the date of interest by defining the day of the year. The six variables previously chosen are then computed. From these variables, the actual vapor pressure (ea), saturation vapor pressure ($esat$), and relative humidity (RH) are calculated using Equations 6.2, 6.3 and 6.4 respectively.

$$ea = 0.6108 \frac{(T_{dew} - 273.15)17.27}{(T_{dew} - 273.15) + 237.3} \quad (6.2)$$

$$esat = 0.6108 \frac{T_{mean}17.27}{T_{mean} + 237.3} \quad (6.3)$$

$$RH = 100 \left(\frac{ea}{esat} \right) \quad (6.4)$$

Where:

- T_{mean} is the mean temperature, being the average between T_{max} and T_{min}

The resulting image is then modified by adding bands for surface solar radiation (R_s), mean wind speed, mean temperature, and relative humidity. Finally, the daily reference evapotranspiration is calculated using a function that takes the day of the year, minimum temperature (T_{min}), maximum temperature (T_{max}), actual vapor pressure (E_a), surface solar radiation (R_s), mean wind speed (u_z), measurement/estimated height for wind speed (z_w), crop coefficient for the day (C_n), and fraction of the daytime during which ET occurs (C_d).

The saturation vapor pressure at the mean temperature ($esat_{tmean}$) is calculated as the average between the saturation vapor pressure at the minimum and maximum temperature, which are calculated by the vapor pressure equation in Equation 6.5.

$$Vaporpressure = 0.6108 \exp\left(\frac{17.27b()}{(b() + 237.3)}\right) \quad (6.5)$$

Where:

- $b()$ represents the temperature value

Equations 6.6, 6.7 and 6.8 represent the slope of the saturation vapor pressure-temperature curve (Δ), psychrometric constant (γ) and net radiation (R_n), respectively. Some other equations are used to get to these, such as cloudiness fraction, clear sky solar radiation, the inverse square of the Earth-Sun distance, sunset hour angle, and Earth inclination.

$$\Delta = \frac{4098esat_{tmean}}{(T_{mean} + 237.3)^2} \quad (6.6)$$

$$\gamma = P_{air}0.000665 \quad (6.7)$$

$$R_n = \frac{R_s 86400}{1000} 0.77 - R_{nl} \quad (6.8)$$

Where:

- R_s is the surface solar radiation.
- R_{nl} is the net long-wave radiation, calculated using actual vapor pressure, cloudiness fraction and, T_{min} and T_{max} in K

Finally, ET_{ref} can be calculated using Equation 6.9

$$ET_{ref} = \frac{0.408 \Delta R_n + \frac{\gamma C_n u_2 (e_{sat} - e_a)}{(t+273)}}{\Delta + \gamma (C_d u_2 + 1)} \quad (6.9)$$

Where:

- u_2 is the wind speed to 2-m based on full logarithmic wind speed profile equation
- $C_n = 900$
- $C_d = 0.34$